Ore Geology Reviews 106 (2019) 446–462

Contents lists available at ScienceDirect

Ore Geology Reviews

journal homepage: www.elsevier.com/locate/oregeorev

Gold behavior in intermediate sulfidation epithermal systems: A case study from the Zhengguang gold deposit, Heilongjiang Province, NE-China

Guoxue Song[a,b,*], Nigel J. Cook[c], Le Wang[a,b], Kezhang Qin[b,a], Cristiana L. Ciobanu[c], Guangming Li[b,a]

[a] University of Chinese Academy of Sciences, 19 Yuanquan Road, Shijingshan, Beijing 100049, China
[b] Institute of Geology and Geophysics, Chinese Academy of Sciences, 19 Beitucheng, Chaoyang, Beijing 100029, China
[c] School of Chemical Engineering, The University of Adelaide, Adelaide, SA 5005, Australia

ARTICLE INFO

Keywords:
Central Asian Orogenic Belt
Zhengguang
Intermediate sulfidation
Epithermal gold deposit
Pyrite
Porphyry system

ABSTRACT

The Zhengguang gold deposit, a typical intermediate-sulfidation epithermal deposit, is located in the southeastern part of the Duobaoshan orefield, west of the Hegenshan-Heihe suture zone, in the eastern part of the Central Asian Orogenic Belt. The deposit comprises five ore zones with total Au reserves exceeding 35 tonnes, with potential additional resources at depth. All vein-type orebodies are hosted by Paleozoic volcanic rocks and comprise multiple vein sets 1–100 cm in thickness. Although gold generally occurs in native form, or as electrum in epithermal deposits like Zhengguang, both pyrite and sphalerite are known to accommodate modest concentrations of invisible gold. This study employs a combination of petrography and sulfide chemistry to determine the role of invisible gold in the Zhengguang ores and the mechanisms of gold incorporation into epithermal sulfides. Three sulfide stages are identified: an early quartz + pyrite (Py1a, Py1b) ± chalcopyrite (Ccp1) stage; a subsequent quartz + sphalerite (Sph2a, Sph2b) + pyrite (Py2a, Py2b, Py2c, Py2d) + chalcopyrite (Ccp2a, Ccp2b) ± galena ± calcite stage; and a late stage containing deformed quartz + pyrite (Py3a, Py3b) ± sphalerite. Petrography and sulfide chemistry allow three groups of pyrite (Au-poor, Au-rich, and a distinct Sb-rich group) to be distinguished, alongside three groups of chalcopyrite (Bi-rich, intermediate-Bi, and Bi-poor), and two groups of sphalerite (Au-poor, Au-rich). A potential porphyry system is indicated beneath the epithermal system by the appearance of Au-poor pyrite and Bi-poor chalcopyrite. After precipitation of early Au-poor sulfides, inflow of relatively low temperature epithermal fluids led to alteration and replacement of early porphyry-related sulfides, and to precipitation of Au-rich pyrite, Bi-rich and intermediate-Bi chalcopyrite, and sphalerite. Gold-rich pyrite contains up to 140 ppm Au, interpreted as both as lattice-scale substitution (Au^{1+}) and as included particles of native gold (Au^0). Epithermal chalcopyrite is an important silver carrier but, although Au is measurable, it is a not a good carrier for gold. A strong positive correlation between Au and Cu in pyrite from the first two stages indicate that gold and other metals were likely sourced from magma-derived hydrothermal fluids. The deposit was formed in the Early Paleozoic but some gold ores appear deformed and partially destroyed by a later metamorphic event during which a distinct Sb-rich pyrite crystallized. This study should catalyze exploration in the orefield as it provides further support for an as-yet undiscovered porphyry system close to the Zhengguang deposit.

1. Introduction

The Central Asian Orogenic Belt (CAOB) extends from the Urals Mountains in Russia in the west, through Kazakhstan, Uzbekistan, Tajikistan, Kyrgyzstan, Xinjiang in northwestern China, parts of Mongolia to Inner Mongolia, and further to Northeast China (Yakubchuk, 2004) (Fig. 1a). It is one of the largest orogenic belts in the world (e.g., Sengör and Burtman, 1993; Jahn et al., 2004; Windley et al., 2007; Xiao and Santosh, 2014; Xiao et al., 2015) and is interpreted to have evolved via accretion of continental blocks, island arcs, and accretionary complexes over a period of more than 800 million years. The CAOB hosts a dense concentration of ore deposits (Buslov et al., 2002; Xiao and Kusky, 2009). These include orogenic gold deposits (e.g., Olympiada, Blagodatnoye, Veduga, Sovetskoe, and Eldorado deposits in Russia with a combined pre-mining resource of almost 2000 t Au; Yakubchuk, 2004; Goldfarb et al., 2014), VMS-type Cu-

* Corresponding author at: University of Chinese Academy of Sciences, 19 Yuanquan Road, Shijingshan, Beijing 100049, China.
E-mail address: sgx@ucas.ac.cn (G. Song).

https://doi.org/10.1016/j.oregeorev.2019.02.001
Received 18 August 2018; Received in revised form 21 January 2019; Accepted 3 February 2019
Available online 05 February 2019
0169-1368/

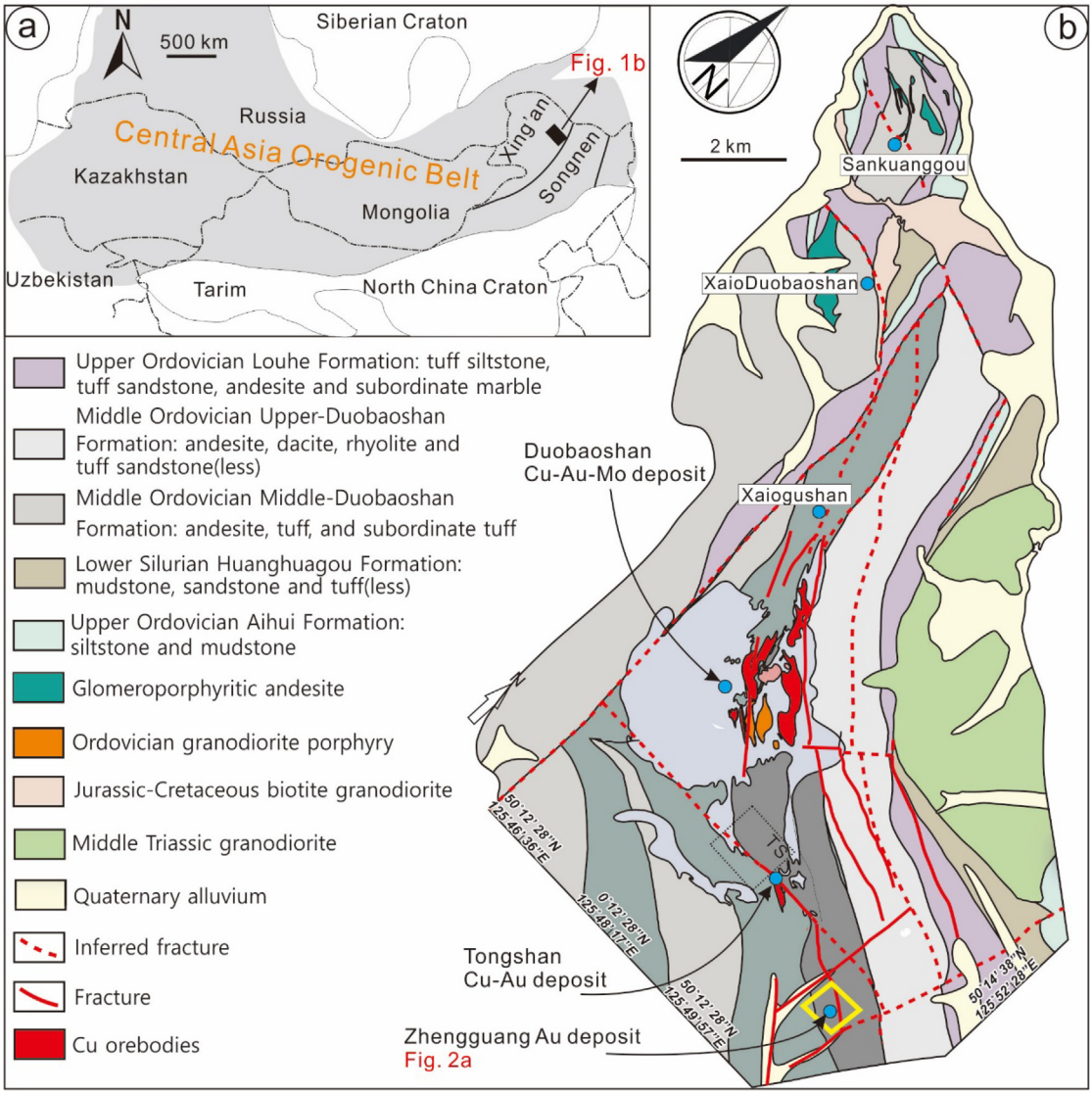

Fig. 1. a) Geological map of the Central Asian Orogenic Belt (CAOB) (modified from Xiao and Kusky, 2009). b) Geological map of the Duobaoshan ore field (modified from Zhao et al., 2018).

Zn-Pb deposits (e.g., A'sele, Keketale, Honghai, and Wulagen in China, Khandiza in Uzbekistan, and Maikain in Kazakhstan; Wan et al., 2010; Lobanov et al., 2014; Mao et al., 2015), porphyry Cu-Mo-Au deposits (e.g., Bozshakol in Kazakhstan; Taldy Bulak in Kyrgyzstan; Oyu Tolgoi and Tsagaan Suvarga in Mongolia; Yubileinoe in Russia; Baogutu, Bainaimiao, Wunugetushan, Duobaoshan, and Tongshan in China; Qin et al., 2002, 2005; Han et al., 2006; Zeng et al., 2014; Mao et al., 2014; Wu et al., 2015), and epithermal Au-Ag-Pb-Zn deposits (e.g., Buerkesidai, Kuoerzhenkuola, A'xi, and Hongshan in NW China, Kubaka, Birkachan, Ol'cha, and Zetin, Russia, and Zhengguang and Sandaowanzi in NE China; Kotlyar et al., 2001; Xu et al., 2006; Shen et al., 2008; Liu et al., 2011; Song et al., 2015; Deng and Wang, 2016).

The Duobaoshan orefield, recognized as the largest concentration of Cu-Au deposits in Northeast China, is located in the eastern part of the CAOB, west of the Hegenshan-Heihe suture zone that separates the Xingan and Songnen Blocks (Fig. 1a). Alongside the well-documented Duobaoshan and Tongshan porphyry Cu-Mo deposits and the Zhengguang epithermal Au deposit, many other hydrothermal vein and porphyry Cu (Mo) occurrences, such as Xiaoduobaoshan, Sankuanggou, and Xiaogushan (Fig. 1b), have been discovered (Song et al., 2015). The Zhengguang gold deposit is positioned in the southeastern part of the Duobaoshan orefield and has a similar, Paleozoic age of ore formation as the well-documented Duobaoshan Cu deposit (Song et al., 2015) (Fig. 1b).

Currently, Zhengguang comprises five ore zones with reserves exceeding 35 metric tonnes Au (Fig. 2a) and remains open at depth. Previous research has focused on the geological characteristics of the deposit, description of the geological setting and characteristics of the orebodies and associated alteration (e.g., Cui et al., 2008; Tong et al., 2015). Several researchers have observed that Zhengguang is closely related to host diorites, the presumed products of Mesozoic magmatism, with fluid inclusion homogenization temperatures (< 300 °C; Deng et al., 2013), indicative of typical epithermal conditions (e.g., Wu et al., 2006; Fu and Yang, 2010; Zhao et al., 2011). Other research has addressed deposit genesis based on geological characteristics (e.g., Gao et al., 2014; Song et al., 2015). These researchers agree that the Zhengguang gold deposit, together with the Duobaoshan and Tongshan copper deposits, formed at 480–452 Ma in an arc setting controlled by subduction of the Paleo-Asian Ocean (e.g., Zeng et al., 2014; Wu et al., 2015). They thus comprise a single evolved metallogenic system spanning porphyry Cu-Au mineralization to epithermal Au mineralization (Song et al., 2015; Wang et al., 2018). Geological features observed at Zhengguang, including the vein sets features, mineral assemblages, alteration types, and low Fe concentration in sphalerite, are

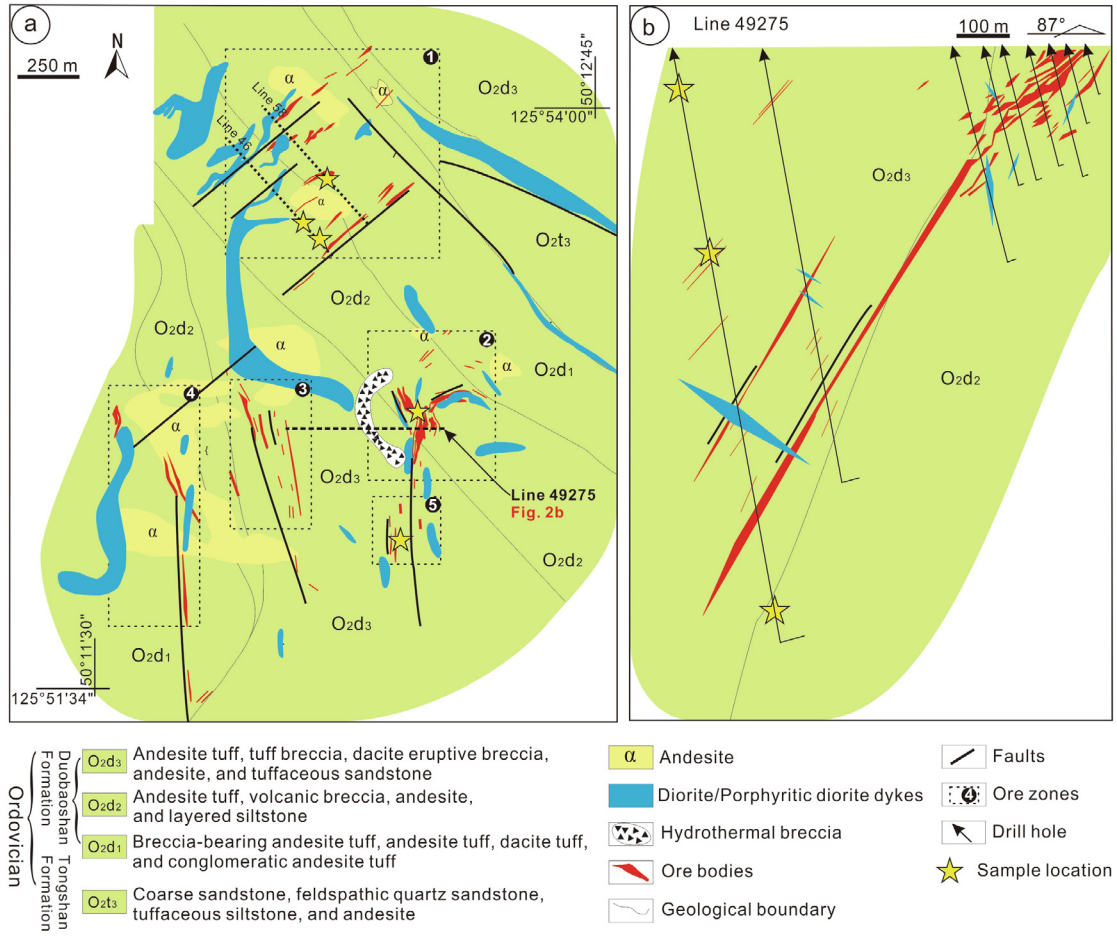

Fig. 2. a) Geological map of the Zhengguang deposit (modified from Song et al., 2015, Wang et al., 2018). b) Cross section of line 49,275 in the No. 2 ore zone from Zhengguang deposit (modified from Song et al., 2015).

consistent with previous studies of other epithermal deposits (Hedenquist et al., 2000; Einaudi et al., 2003; Sillitoe and Hedenquist, 2003), indicating that Zhengguang is an intermediate-sulfidation epithermal gold deposit (Song et al., 2015, 2018; Wang et al., 2018).

Base metal sulfides (chalcopyrite and sphalerite) are, together with pyrite, the most abundant minerals in the Zhengguang resource and display a wide range of ore textures. In many porphyry and epithermal systems, the trace element composition of common sulfides has been shown to be a valuable tool to constrain ore genesis, with a significant change in trace element composition from porphyry to epithermal environments (Large et al., 2009; Reich et al., 2013a; Deditius et al., 2014; Franchini et al., 2015; Song et al., 2018). Prior to the present study, little research has focused on sulfide mineralogy, or the potential use of mineral geochemistry to constrain ore genesis, either at Zhengguang, or within the greater Duobaoshan orefield.

In this study, concentrations of Au and other trace elements have been determined in sulfides from well-constrained samples from Zhengguang using laser ablation-inductively coupled plasma mass spectrometry (LA-ICP-MS). We show that trace element distributions within pyrite, sphalerite, and chalcopyrite can help identify different stages of alteration, replacement, and deformation, and furthermore demonstrate the role played by these minerals as Au-carriers in the deposit. Based on the trace element dataset, and in light of recent studies documenting the geochemical behavior of Au, As, Te and Cu in hydrothermal systems (e.g., Reich et al., 2013a; Deditius et al., 2014), we go on to explore the possible relationship between porphyry- and epithermal-style mineralization.

2. Geological setting and characteristics

2.1. Lithostratigraphic sequence

Previously published research (e.g., Wu et al., 2006; Zeng et al., 2014; Tong et al., 2015; Song et al., 2015; Wang et al., 2018) showed the lithostratigraphic sequence in the orefield to be composed of the Middle Ordovician Tongshan and Duobaoshan Formations (Figs. 1b and 2a). The Tongshan Formation is restricted to the northern part of the orefield. Major lithologies are coarse sandstone, feldspathic quartz sandstone, and tuffaceous siltstone. The Duobaoshan Formation, which is composed of a series of volcanic rocks with different lithofacies, occurs throughout the orefield and is the major ore-hosting strata (Song et al., 2015). Dominant lithologies include andesite tuff, conglomeratic andesitic tuff, and andesite, but also include airfall volcanics, lava overflow, volcanic debris flow, and volcanic sedimentary facies (Fig. 2a). Explosive and eruptive facies are interbedded with one other and show that volcanic activity alternated between eruption of lava and pyroclastic rocks during the outbreak of volcanic activity (Song et al., 2015). Based on the spatial distribution and variation characteristics of ignimbrites, volcanic breccias, volcanic-pyroclastic rocks, Song et al. (2015) speculate on the existence of a Paleozoic paleo-volcano edifice within the district.

2.2. Structural geology

The Duobaoshan region has experienced multiple tectonic movements through time and is characterized by a series of NNE-SSW-, NE-

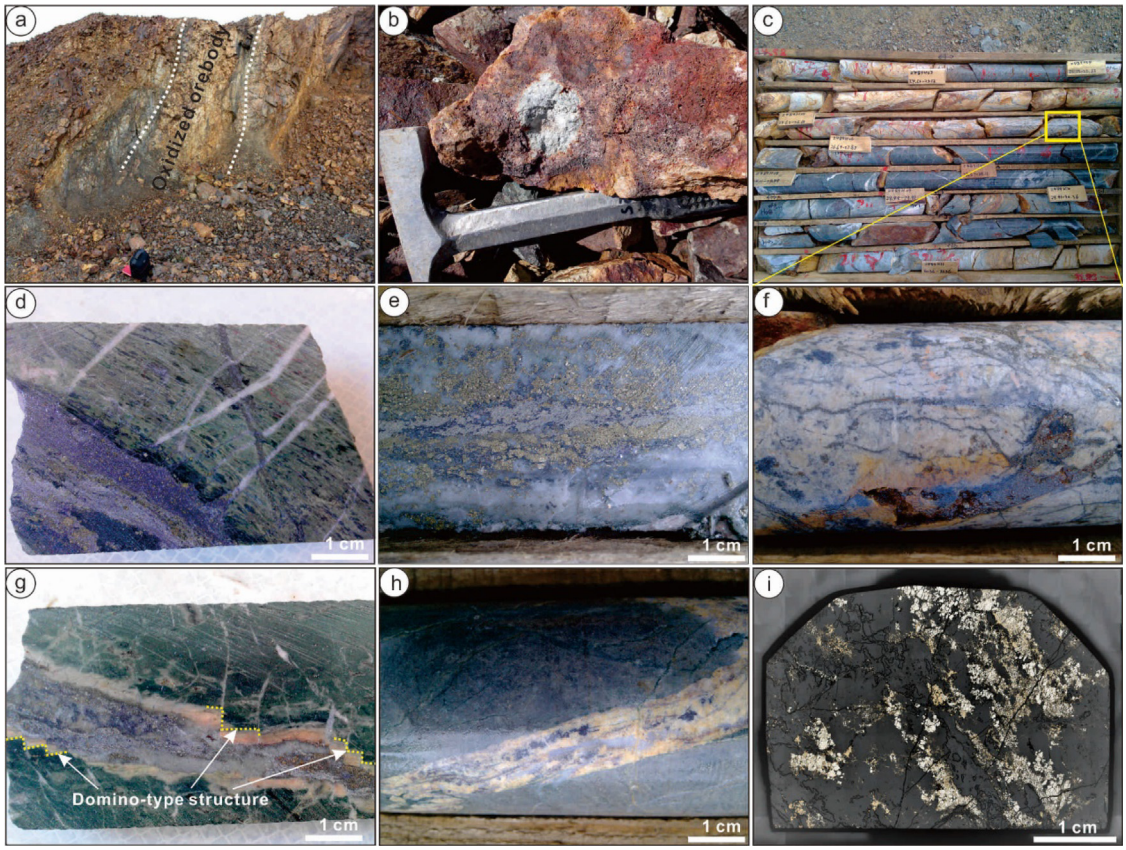

Fig. 3. a) Field photograph of the oxidized ore body; b) Photo of oxidized ore with ferrohydrite and jarosite; c) Drill cores with epidote-chlorite-calcite ± pyrite alteration; d) Vein-type gold ore, composed of sphalerite, chalcopyrite, and pyrite; e) Vein-type gold ore, composed of sphalerite and pyrite; f) Pyrite vein in gold ore, from the drill core shown in (c); g) Deformed sphalerite-chalcopyrite-pyrite ore with Domino-type structure; h) Quartz-calcite-hematite vein; i) Porphyry related quartz-calcite-hematite vein.

SW-, and minor E-W- and N-S-trending structures (Li et al., 2008; Hao et al., 2015) (Fig. 1b). In the Duobaoshan and Tongshan ore districts, NE-trending faults pre-date mineralization, whereas NW-trending faults are main structures and control the distributions of the Duobaoshan and Tongshan deposits (Du et al., 1988; Han et al., 2007). The EW-trending faults are post-mineralization in age and disrupt orebodies (Wu et al., 2015) (Fig. 1b). Distinct from the Duobaoshan and Tongshan deposits, gold mineralization in Zhengguang occurs not only along the NW-trending Sankuanggou-Duobaoshan structural belt but also along NS-trending and NE-trending faults (Li et al., 2008; Song et al., 2015) (Fig. 2a). Gold orebodies in the No. 1 ore zone are controlled by NE-trending faults, orebodies from the No. 2 ore zone are controlled by NW-, NE- and NS-trending faults, whereas orebodies from the Nos. 3, 4 and 5 ore sectors are controlled by NW- and NS-trending faults (Fig. 2a) (Tong et al., 2015).

2.3. Magmatic rocks

The dominant intrusive rocks are diorite, porphyritic diorite, porphyritic granodiorite, and porphyritic monzonite (Wang et al., 2018). The diorite and porphyritic diorite rocks occur across the whole district and tend to occur at intersections between the NW-trending compression and scissor fault zones and NE-trending tenso-shear faults (Tan et al., 2010; Fig. 2a). These are irregular, elliptical in shape at surface, and intruded Paleozoic volcanic rocks and porphyritic granodiorite, as well as the Au-bearing orebodies (Song et al., 2015). The latter authors report zircon U-Pb ages between 280 and 297 Ma from porphyritic diorite, indicating a latest Permian magmatic event after formation of the Zhengguang deposit. The porphyritic granodiorite and porphyritic monzonite rocks are restricted to deep levels of the No. 1 ore zone. These have zircon U-Pb ages of 436.1 ± 1.6 Ma and 454.6 ± 1.4 Ma, respectively (Song et al., 2015). Drillcore observations clearly show that they intruded volcanic rocks and cut off or ruptured the Au-bearing orebodies with evidence of minor clay alteration, chloritization, and carbonatization. Field relationships between volcanic rocks, diorite, porphyritic diorite, porphyritic granodiorite, and porphyritic monzonite indicate that all intrusive rocks in the district are younger than the volcanic rocks and the Au-bearing orebodies (Song et al., 2015; Wang et al., 2018).

2.4. Alteration

Wall-rock alteration is well developed in the Zhengguang deposit, with two phases of alteration zones observed from orebodies to wall rocks: the early phase is characterized by planar epidote-chlorite-calcite ± pyrite alteration in andesitic volcanic rocks, and the latter by linear zones of quartz-sericite-illite-calcite alteration adjacent to orebodies within the volcanic rocks. The epidote-chlorite-calcite ± pyrite alteration is the most widely observed type of alteration in the Duobaoshan orefield and is recognized across a 30 km^2 area (Du et al., 1988). The latter authors regarded propylitization (epidote-chlorite-calcite ± pyrite alteration) as a 'background' alteration affecting volcanic rocks, Paleozoic granodiorite and porphyritic granodiorite alike. Within this alteration zone, K-feldspar is variably sericitized or epidotized, hornblende is partially or totally replaced by chlorite and epidote, and biotite shows partial or total chloritization. Epidote occurs in varying abundance, replacing primary hornblende, or forming mm-thick veins in association with calcite and fine-grained chlorite. Most pyrite is either euhedral and disseminated within the rock groundmass, or appears as veinlets in andesite rocks (Song et al., 2015). The quartz-

sericite-illite-calcite alteration zone is developed within tens of meters on either side of the orebodies and is closely associated with gold mineralization (Song et al., 2015; Wang et al., 2018).

2.5. Ore bodies, ore types, and ore mineral assemblages

About 190 Au-bearing orebodies have been discovered in five ore zones, with an average Au grade of 3.25 g/t. All orebodies occur within Paleozoic volcanic rocks and comprise multiple hydrothermal veins 1–100 cm in thickness and 5–20 m in strike length (Song et al., 2015) (Fig. 2a). The No. 1 and 2 ore zones are the most significant and together comprise > 175 orebodies. The No. 1 ore zone, located in the northwestern part of the ore district, comprises NE-trending Au ores (Fig. 2a). The No. 2 ore zone (the largest, with a total Au reserve exceeding 23 tonnes), is located in the southeastern part of the ore district within a "Y-shaped" configuration (Fig. 2a). Ore zones No. 3, 4, and 5 are relatively small and occur in the west of the ore district (Fig. 2a).

Gold ores can be classified into two types: primary ores (Fig. 3c–g); and oxidized ores (Fig. 3a, b). Primary ores are of vein type, with base metal minerals disseminated within quartz and quartz-calcite veins. Primary ores can be sub-divided according to the prevailing mineral assemblages into: vein type quartz-pyrite-sphalerite-galena ores; vein type pyrite-sphalerite ores; and vein type pyrite ores. Oxidized ores are particularly well developed at shallow depths in the No. 2 ore zone, where they display yellow to yellowish-brown colors (Fig. 3a, b), and are formed by weathering on primary ores with widespread ferrohydrite and jarosite (Fig. 3b).

Ore mineral assemblages comprise dominant pyrite, chalcopyrite, galena, sphalerite, and hematite, with minor Cd-bearing sphalerite, tetrahedrite, argentite, native gold, electrum, and hessite (Song et al., 2015) (Table 1; Fig. 4a–p). Minerals particularly closely associated with gold are pyrite, chalcopyrite, galena, and sphalerite. Parts of the ore displaying gold enrichment characteristically have high contents of sphalerite and chalcopyrite. Gold-bearing minerals are dominated by native gold (accounting for 86.1%), with minor electrum (accounting for 13.9%). Coarse-grained gold (> 74 μm) accounts for 2.3% of the visible gold in the deposit, medium-grained gold (37–74 μm) accounts for 17.9%, fine-grained gold (10–37 μm) accounts for 58.8%, and micro-sized (< 10 μm) accounts for 21.1% (Wang and Zhou, 2009).

3. Samples and experimental methods

Eight representative samples were selected and analyzed (Table 2). Each was prepared as a 1-inch polished block and characterized by reflected light microscopy and backscattered electron (BSE) imaging prior to LA-ICP-MS analysis. Only areas of sulfide grains free of noticeable inclusions were selected for LA-ICP-MS analysis. Samples 49275-2-1235, 49275-2-469, 49275-2-78, and 263-257 are taken from the No. 2 ore zone, samples 46-7-285, 46-7-548, and 58-8-518 are from the No. 1 ore zone, and sample 58-2-616 was taken from the No. 5 ore zone. In this study, we focus on sulfides from the three distinct mineralization stages. A detailed description of samples is given in Table 1. Sample 49275-2-1235 is from an early quartz-pyrite vein with abundant early pyrite (Figs. 4a and 5a; Table 2). The sample was collected at a depth of 1235 m from drillhole 49275-2 in the No. 2 ore zone (first mineralization stage). Samples 58-2-616, 46-7-285, 46-7-548, 58-8-518, 263-257, and 49275-2-469 are from quartz-polymetallic sulfides-calcite veins (Fig. 4b-p, 5b-c, and 6d-f; Table 2). Among them, the first three are from drillcore intersecting the No. 1 ore zone, whereas 263-257 was taken from drillhole 263 (No. 2 ore zone), 49275-2-469 was taken from a depth of 469 m in drillhole 49275-1 (No. 2 ore zone), and sample 58-2-616 was taken from a depth of 616 m deep in drillhole 58-2 (No. 5 ore zone) (Table 2). Sample 49275-2-78 is a deformed quartz-polymetallic sulfide-calcite vein representing the third mineralization stage (Fig. 4g; Table 2).

LA-ICP-MS analysis was carried out using a Resonetics M-50-LR

Table 1
Summary of ore mineral assemblages and abbreviations used.

Stages	typical veins	pyrite	chalcopyrite	sphalerite	galena	tetrahedrite	hematite	electrum	hessite	argentite
Early quartz + pyrite ± chalcopyrite stage	quartz-pyrite veins	Py1a								
	quartz-pyrite-chalcopyrite veins	Py1b	Ccp1							
Second quartz + sphalerite + pyrite-chalcopyrite ± galena ± calcite stage	quartz-pyrite-chalcopyrite veins	Py2a	Ccp2a			Tet			Hes2a	Arg
	quartz-pyrite-chalcopyrite-sphalerite-galena veins	Py2b	Ccp2b	Sph2a	Gn2a				Hes2b	
	quartz-pyrite-sphalerite-calcite veins	Py2c		Sph2b	Gn2b			El		
	quartz-pyrite veins	Py2d								
	quartz-calcite-pyrite-hematite veins	Py					Hem			
Late deformed quartz + pyrite ± sphalerite stage	quartz-pyrite veins	Py3a/Py3b								

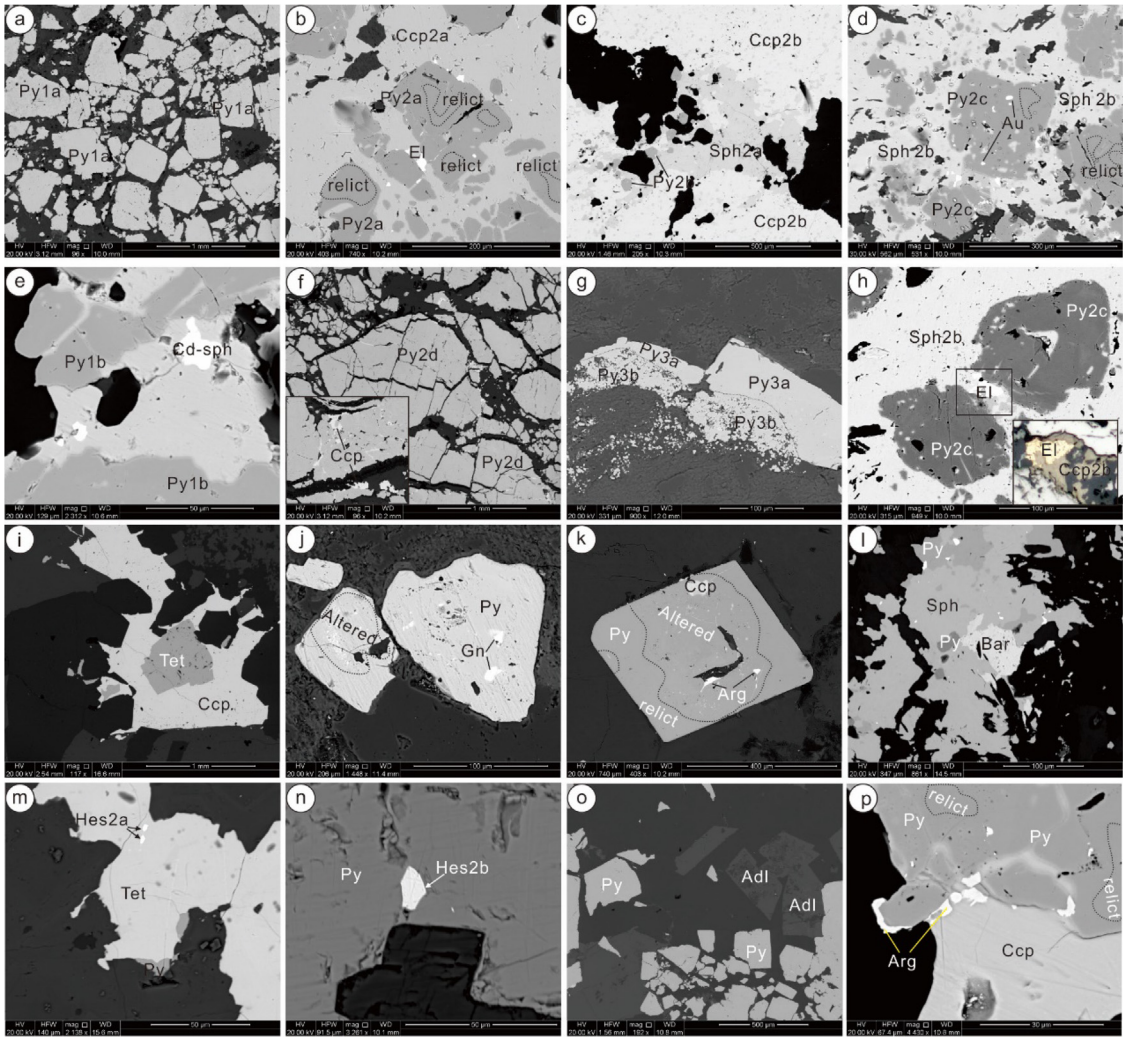

Fig. 4. Back-scattered electron (BSE) images (a-l) showing sulfides from Zhengguang. a) Euhedral-subhedral pyrite from the first sulfide stage (Py1a) with slight alteration and no fracturing. b) Chalcopyrite (Ccp2a) from the second stage overprinting primary pyrite, and formation of Py2a. Electrum is observed within and surrounding replaced pyrite. c) Second-stage chalcopyrite (Ccp2b) and sphalerite (Sph2a) overprinting primary pyrite, and formation of Py2b. d) Second stage sphalerite (Sph2b) overprinting primary pyrite and forming Py2c. Electrum is observed enclosed within or around replaced pyrite. e) Chalcopyrite (Ccp1) replacing primary pyrite. Cd-bearing sphalerite is included within chalcopyrite. f) Fractured pyrite (Py2d) overprinted by sphalerite and chalcopyrite. g) Primary pyrite displaying a metamorphic overprint, forming Py3a (slightly altered pyrite) and Py3b (strongly altered pyrite), Py3b is recrystalized as small pyrite (sub)-grains. h) Second stage sphalerite (Sph2b) overprinting primary pyrite and forming Py2c; note electrum within sphalerite. i) Tetrahedrite included in chalcopyrite. j) Euhedral pyrite replaced by galena. k) Euhedral pyrite replaced by chalcopyrite and argentite. l) Primary pyrite replaced by sphalerite and barite. m) Hessite included within tetrahedrite. n) Hessite included within pyrite. o) Euhedral adularia coexisting with euhedral to subhedral pyrite. p) Chalcopyrite replacing primary pyrite with argentite inside or surrounding the pyrite. Adl-adularia, Arg-argentite, Bar-barite, Ccp-chalcopyrite, El-electrum, Hes-hessite, Gn-galena, Py-pyrite, Sph-sphalerite, Tet-tetrahedrite. 'Relict' refers to preserved or slightly replaced primary pyrite.

193 nm Excimer laser attached to an Agilent 7700cx Quadrupole ICP mass spectrometer (Adelaide Microscopy, The University of Adelaide). The Resonetics laser designed by Laurin Technic Pty. uses a two-volume ablation cell for outstanding trace element sensitivity, washout, and stability (Müller et al., 2009). The ablation cell is filled with UHP He (0.7 l/min), which is mixed with Ar (0.93 l/min) after leaving the cell and is directly introduced to the torch through a "squid" (pulse homogenizing device). The ICP-MS is calibrated regularly to maximize sensitivity, whilst keeping production of molecular oxide species (i.e., $^{232}Th^{16}O/^{232}Th$) and doubly charged ion species (i.e., $^{140}Ce^{2+}/^{140}Ce^{+}$) as low as possible, and typically < 0.2%.

Laser beam energy output was set at 100 mJ at a 35 μm spot size using a repetition rate of 10 Hz. Each analysis comprised a 30 s background measurement followed by 35 s of sample ablation, while a 30 s delay was allowed after each spot analysis to ensure adequate cell wash-out, gas stabilization, and computer processing time. Analyzed isotopes include ^{34}S, ^{55}Mn, ^{57}Fe, ^{59}Co, ^{60}Ni, ^{65}Cu, ^{66}Zn, ^{69}Ga, ^{75}As, ^{82}Se, ^{95}Mo, ^{107}Ag, ^{111}Cd, ^{115}In, ^{118}Sn, ^{121}Sb, ^{125}Te, ^{182}W, ^{197}Au, ^{202}Hg, ^{205}Tl, ^{206}Pb, ^{207}Pb, ^{208}Pb and ^{209}Bi. Dwell times for In, Au and Tl were set to 0.05 s, while all other elements were set to 0.01 s. Mean errors and the minimum detection limits for common trace elements in each sample are provided as Electronic Appendix B. The latest MASS-1 certificate of analysis (United States Geological Survey, 2014) is used. Pyrite, sphalerite, and chalcopyrite were analyzed by EPMA and thus values of 44.975 wt% Fe, 65.697 wt% Zn, and 34.017 wt% Cu were used as internal standards. GLITTER data reduction software (Van Achterbergh et al., 2001) was used to carry out data calculations.

4. Results

4.1. Sulfide petrography

Consideration of vein relationships in the field and among co-existing minerals under the microscope allows identification of three

Table 2
Summary table describing samples selected for LA-ICP-MS analysis.

Sample no.	Ore zone	Location and depth	Sulfide stages	Vein width	Generations of sulfides
49275-2-1235	no. 2	1235 m, drillhole ZK49275-2	Early quartz-pyrite ± chalcopyrite stage	25 mm	pyrite (Py1a)
58-2-616	no. 5	616 m, drillhole ZK58-2	Early quartz-pyrite ± chalcopyrite stage	30 mm	pyrite (Py1b), chalcopyrite (Ccp1)
46-7-285	no. 1	285 m, drillhole ZK46-7	Second quartz-sphalerite-pyrite-chalcopyrite ± galena ± calcite stage	30 mm	pyrite (Py2a), chalcopyrite (Ccp2a)
46-7-548	no. 1	548 m, drillhole ZK46-7	Second quartz-sphalerite-pyrite-chalcopyrite ± galena ± calcite stage	25 mm	pyrite (Py2b), chalcopyrite (Ccp2b), Sphalerite (Sph2a)
58-8-518	no. 1	518 m, drillhole ZK58-8	Second quartz-sphalerite-pyrite-chalcopyrite ± galena ± calcite stage	15-25 mm	pyrite (Py2c), sphalerite (Sph2b)
263-257	no. 2	257 m, drillhole ZK263	Second quartz-sphalerite-pyrite-chalcopyrite ± galena ± calcite stage	20 mm	pyrite (Py2c), sphalerite (Sph2b)
49275-2-469	no. 2	469 m, drillhole ZK49275-2	Second quartz-sphalerite-pyrite-chalcopyrite ± galena ± calcite stage	20 mm	pyrite (Py2d)
49275-2-78	no. 2	78 m, drillhole ZK49275-2	Late deformed quartz-pyrite ± sphalerite stage	1–10 mm	pyrite (Py3a, Py3b)

sulfide stages (Song et al., 2015) (Table 1): an early quartz + pyrite ± chalcopyrite stage; a second quartz + sphalerite + pyrite + chalcopyrite ± galena ± calcite stage; and a late deformed quartz + pyrite ± sphalerite stage. Based on observation of the three sulfide stages, seven texturally distinct generations of pyrite can be recognized. Py1a and Py1b are from quartz-pyrite veins belonging to the first stage. Py1a is euhedral without evidence for significant alteration or replacement (Figs. 4a and 5a; Table 1), and Py1b are altered by Ccp1 in quartz-pyrite-chalcopyrite veins (Fig. 4e; Table 1). Sub-types Py2a though Py2d belong to the second stage, and coexist with epithermal base metal sulfides, sphalerite, galena, and chalcopyrite (Figs. 4-6; Table 1). A majority of the Stage 2 pyrites formed during a replacement event in which epithermal fluids reacted with early Py1. Py3 is from syn-deformational quartz-polymetallic sulfide veins of the third stage (Fig. 4g; Table 1). Moreover, two phases of sphalerite (Sph1 and Sph2) and three phases of chalcopyrite (Ccp1, Ccp2a and Ccp2b) can be readily recognized (Figs. 4, b-p; 5b-c and 6d-f; Table 1). Sph2a, Sph2b, Ccp2a and Ccp2b are from the second stage veins and coexist with Py2a, Py2b, Py2c or Py2d, whereas Ccp1 is from the first stage and coexist with early Py1b (Fig. 4e). In the first stage, euhedral, coarse-grained pyrite (Py1a) is the main sulfide in the epidote-chlorite-calcite ± pyrite alteration halo (Figs. 4a and 5a). During superposition by subsequent epithermal fluids, relicts of early (Py1a) pyrite are preserved within Au-rich sulfides (e.g., Fig. 4b, d, j, k, p).

The second stage represents the main epithermal gold mineralization stage, and resulted in subhedral Au-bearing pyrite, sphalerite, chalcopyrite, and galena. This type of gold mineralization overprints earlier alteration via replacement of early pyrite. Observations in reflected light and back-scatter electron imaging show that epithermal pyrite (Py2a through Py2d; Figs. 4b-e, h, p, 3b-c and 4d-f), sphalerite (Sph2a and Sph2b; Figs. 4b-f, h, i, 5c and 6d-f), chalcopyrite (Ccp2a and Ccp2b; Figs. 4b–c, e, and 5b-c), and galena replace and alter Py1a (Fig. 4j).

Two types of pyrite (Py3a and Py3b) are identified from the third stage. The former resembles second-stage pyrite but with slight deformation (Fig. 4g), whereas Py3b is recrystallized pyrite from broken Py2 in the form of small grains under heavy deformation (Fig. 4g). Py3b is generally porous and may contain abundant 1–2 μm-sized pores (Fig. 4g).

4.2. Compositional data for sulfides

To constrain ore genesis, we have mainly focused on the distributions of Au, Ag, Te, Sb, As, Bi, Hg, Pb, Zn, Cu and Mo in pyrite, Au, Ag, Zn, Te, Sb, As, Bi, Hg, Pb and Mo in chalcopyrite, and Au, Ag, Te, Sb, As, Bi, Hg, Pb, Cu, Mo, and Fe in sphalerite.

4.2.1. Pyrite

Trace elements were analyzed in pyrite from eight samples (361 spot analyses after careful quality control checks). Three distinct groups of pyrite data are identified from the eight texturally distinct generations: a Au-poor group, a Au-rich group; and a distinct Sb-rich group.

Gold-poor pyrite is present in many samples (Table 2). The distinct feature is that almost all pyrite appears unaltered or only slightly altered (Fig. 4a-k and 5a-c, d-f). Gold-poor, slightly altered pyrite can be often found as relicts (Fig. 4b-k and 5b-c, d-f) within Au-rich pyrite. Compared to other groups, Au-poor pyrite (< 2 ppm, mean 0.66 ppm) also contains the least Ag (< 100 ppm, mean 5.9 ppm), Sb (< 243 ppm, mean 5.1 ppm), As (< 3000 ppm, mean 986 ppm), and Cu (< 2000 ppm, mean 407 ppm) (Table 3). Figs. 7 and 8 show the positive correlations between Au and the trace elements As, Bi, Ag, Sb, Cu, and Te in Au-poor pyrite.

Gold-rich pyrite is mainly of types Py2a through Py2d (Tables 3, Supplement 1). Among these, Py2a only coexists with Ccp2a, Py2b only coexists with Ccp2b and Sph2, Py2c only coexists with Sph2b, and Py2d is fractured and coexists with minor sphalerite (Figs. 4b-k and 5b-f).

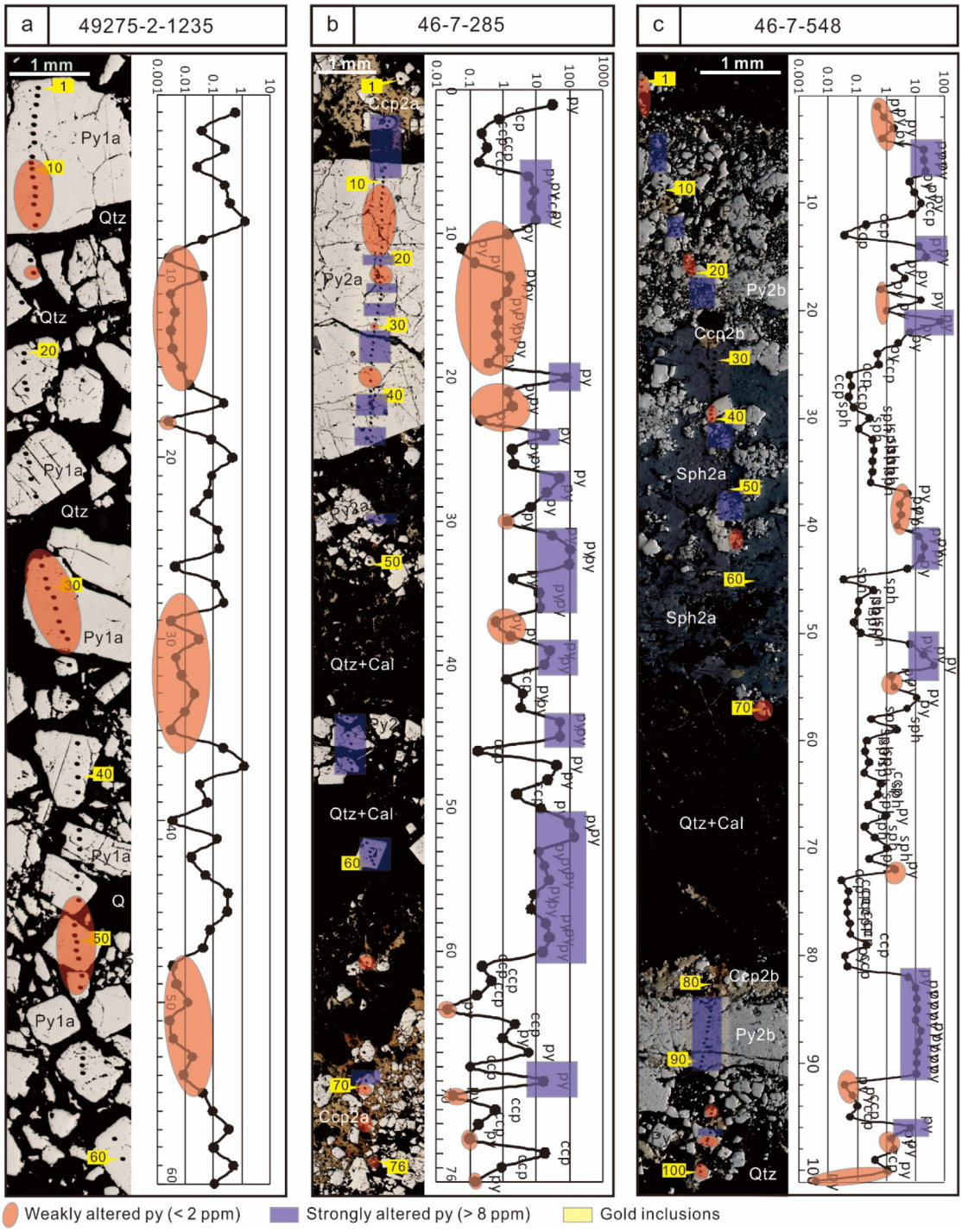

Fig. 5. Reflected light microphotographs of sulfides, showing locations of LA-ICP-MS analysis spots and measured Au contents. a) sample 49275-2-1235, dominated by first-stage euhedral pyrite (Py1a) recognizable by low Au concentration. b) sample 46-7-285, dominated by second-stage pyrite (Py2a) and chalcopyrite (Ccp2a). Strongly altered pyrite can be recognized by higher Au (mostly > 8 ppm). c) sample 46-7-548 mostly features second-stage pyrite (Py2b), chalcopyrite (Ccp2b) and sphalerite (Sph2a). Strongly altered pyrite can also be recognized by higher Au content. Py-pyrite, Ccp-chalcopyrite, Sph-sphalerite.

Almost all Au-rich pyrite pyrite (up to 140 ppm, mean 13.9 ppm) is strongly replaced by sphalerite, galena, chalcopyrite, or other minor minerals (Figs. 4b-k and 5b-f). This group of pyrite also contains the most Ag (up to 1290 ppm, mean 116 ppm), As (up to 10,000 ppm, mean 3212 ppm), and Cu (up to 5000 ppm, mean 1912 ppm) (Table 3). Figs. 7 and 8 show the positive correlation between Au and As, Bi, Ag, Sb, Cu, and Te in Au-rich pyrite.

Antimony-rich pyrite belongs exclusively to the third stage and formed via metamorphic overprinting of Py2 in sample 49275-78 (Table 2). Py3 is strongly altered and present only as relicts (Fig. 4g). This group of pyrite contains the most Sb (up to 69.2 ppm, mean 29.2 ppm) but conspicuously low concentrations of Te (< 0.75 ppm, mean 0.48 ppm) and Bi (< 0.49 ppm, mean 0.21 ppm) (Table 3). Figs. 8 and 9 show the negative correlation between Au and Ag, Mo, Te, and Sb in Sb-rich pyrite, and the positive correlation between Au and As.

4.2.2. Chalcopyrite

Trace elements were analyzed in chalcopyrite from three samples

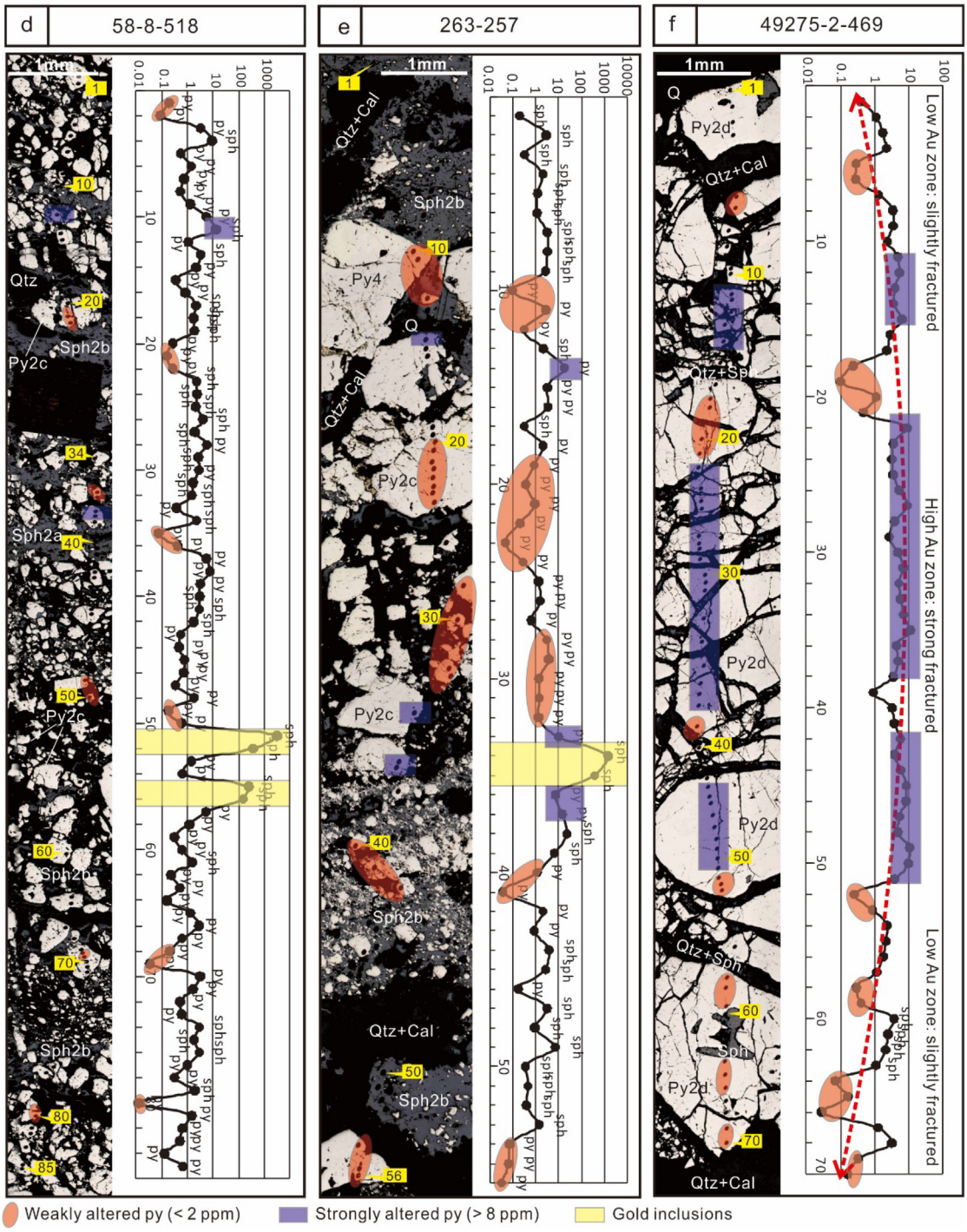

Fig. 6. Reflected light microphotographs of sulfides, showing locations of LA-ICP-MS analysis spots and measured Au contents. d) sample 58-8-518 includes pyrite (Py2c) and sphalerite (Sph2b). Relict pyrite is recognizable by low Au concentrations (mostly < 2 ppm), whereas younger pyrite typically contains higher Au (mostly > 8 ppm). Electrum may occur as inclusions in sphalerite. Euhedral pyrite is also replaced and broken up into relict sub-grains by sphalerite. e) sample 263-257 containing pyrite (Py2c) and sphalerite (Sph2b). Euhedral pyrite is replaced by sphalerite and is preserved as relict sub-grains; note electrum inclusions within sphalerite. f) sample 49275-2-469 contains fractured and replaced pyrite (Py2d). Au contents gradually increase from the rim to the pyrite grain core, the. Points within the core show strong alteration and > 8 ppm Au). Py-pyrite, Ccp-chalcopyrite, Sph-sphalerite.

(48 spot analyses in total). Due to the large variation range of Bi, the data are sub-divided into three groups: Bi-rich; intermediate-Bi; and Bi-poor (Table 3; Fig. 8h). The first two groups are from epithermal gold mineralization. The Bi-rich group are also enriched in Au and Te and are from Ccp2a (sample 46-7-285) (Table 2; Table 3; Supplement 2), which replaces Py2a, and does not co-exist with sphalerite. They contain 0.1–17.9 ppm Au (mean 2.0 ppm), 3.7–270 ppm Ag (mean 59.7 ppm), and the highest concentration of Bi (mean 80 ppm) (Table 3). The intermediate-Bi group is from Ccp2b (sample 46-7-485 ppm), which replaces Py2b, and co-exists with sphalerite. These contain 0.03–0.40 ppm Au (mean 0.08 ppm), 28–959 ppm Ag (mean 124 ppm), 0.56–16 ppm Te (mean 3.7 ppm), intermediate levels of Bi (mean 13.4 ppm) and the lowest concentration of Zn (mean 30.8 ppm) (Table 3). The Bi-poor group (0.05–10.6 ppm, mean 0.97 ppm) is from Ccp1 (sample 58-2-616), which replaces Py1b and coexists with minor sphalerite (Fig. 4; Table 3). Their chemistry resembles chalcopyrite

Table 3
Summarised results of *in-situ* LA-ICP-MS data of sulphides (pyrite, sphalerite, chalcopyrite; values in ppm.

Minerals	Groups	Phases		Au	Ag	Te	Sb	As	Bi	Hg	Pb	Zn	Cu	Mo	Fe
Pyrite	Au-poor pyrite	Includes Py1a, Py1b, and a portion of Py2a, Py2b, Py2c, Py2d (Au < 2 ppm) (Samples 49275-1-1235, 58-2-616, 46-7-285, 46-7-548, 263-257, 58-8-518)	Min	0.01	0.01	0.29	0.04	6.98	–	0.08	0.02	0.95	0.61	0.02	–
			Max	1.85	107	243	94.3	6804	43.1	2.17	2157	28,027	8838	8.30	–
			Mean (n = 207)	0.66	5.89	12.0	5.06	986	2.52	0.17	121	940	407	0.43	–
			St. Dev.	0.18	0.99	3.35	0.46	124	0.27	0.06	30.1	88.5	61.0	0.07	–
	Au-rich pyrite	Includes a portion of Py2a, Py2b, Py2c, Py2d, and Py3a (Au > 2 ppm) (Samples 46-7-285, 46-7-548, 263-257, 58-8-518, 49275-1-469, 49275-1-78)	Min	2.01	0.15	0.24	0.03	13.3	–	0.07	1.24	0.89	4.97	0.02	–
			Max	140	1290	1237	146	12.347	1599	2.31	2771	56.862	9713	177	–
			Mean (n = 139)	13.9	116	126	10.4	3212	38.7	0.20	287	1686	1121	3.77	–
			St. Dev.	3.00	16.1	30.1	0.71	333	4.38	0.06	95.4	188	131	0.35	–
	Sb-rich pyrite	Includes Py3b (Sample 49275-1-78)	Min	0.34	5.69	0.19	1.82	659	0.02	0.09	27.5	3.77	46.8	0.06	–
			Max	5.68	68.1	0.75	69.2	9428	0.49	0.36	429	1589	8735	86.6	–
			Mean (n = 13)	3.27	37.6	0.48	29.2	3234	0.21	0.18	164	218	1912	8.46	–
			St. Dev.	0.21	1.62	0.15	1.12	286	0.02	0.07	13.9	11.1	96.4	0.45	–
Chalcopyrite	Bi-rich chalcopyrite	Includes Ccp2a (Sample 46-7-285)	Min	0.11	3.68	2.44	0.51	2.60	37.3	1.04	28.2	11.8	–	0.22	–
			Max	17.9	270	263	7.21	12.8	190	3.47	157	184	–	2.18	–
			Mean (n = 17)	2.03	59.7	38.8	1.57	4.60	79.9	1.74	54.6	37.0	–	0.53	–
			St. Dev.	0.52	5.66	12.2	0.37	1.97	8.84	0.66	40.3	8.9	–	0.24	–
	Intermediate-Bi chalcopyrite	Includes Ccp2b (Sample 46-7-548)	Min	0.03	21.9	0.56	0.91	3.06	0.81	1.11	8.2	12.7	–	0.43	–
			Max	0.40	959	16.0	208	115	79.9	5.87	298	103	–	3.53	–
			Mean (n = 12)	0.08	124	3.67	22.9	16.8	13.3	2.35	45.6	30.8	–	0.87	–
			St. Dev.	0.03	16.6	1.52	3.86	4.13	1.72	0.76	10.2	9.2	–	0.30	–
	Bi-poor chalcopyrite	Includes Ccp1 (Sample 58-2-616)	Min	0.05	13.5	0.54	0.39	1.34	0.05	0.94	1.2	6.4	–	0.64	–
			Max	0.09	191	3.40	13.1	13.2	10.6	1.31	231	241	–	1.10	–
			Mean (n = 15)	0.06	53.0	2.19	5.19	6.03	0.97	1.10	68.6	60.8	–	0.90	–
			St. Dev.	0.03	5.43	1.10	0.88	1.85	0.15	0.52	12.0	10.3	–	0.40	–
sphalerite	Au-poor sphalerite	Includes Sph2a (Sample 46-7-548)	Min	0.03	12.8	0.05	0.55	0.32	0.90	38.2	6.41	–	73.9	0.03	561
			Max	1.02	148	36.0	8.84	2.87	159	46.0	8136	–	3902	0.72	4659
			Mean (n = 23)	0.27	40.1	4.48	3.19	1.29	13.3	42.4	733	–	1052	0.15	1608
			St. Dev.	0.06	5.68	1.04	0.25	0.23	1.18	4.50	105	–	122	0.04	104
	Au-rich sphalerite	Includes Sph2b (Samples 263-257, 58-8-518)	Min	0.20	5.32	0.23	0.58	1.17	0.16	2.47	17.9	–	14.7	0.01	258
			Max	13.2	198	96.3	11.0	61.2	2.80	52.1	206	–	274	6.03	77,397
			Mean (n = 39)	2.60	37.5	18.5	4.46	7.39	0.77	28.7	65.7	–	91.8	0.44	11,181
			St. Dev.	0.85	6.25	6.37	0.47	1.14	0.11	4.42	34.4	–	14.9	0.07	1237

Notes: Min = minimum; Max = maximum; St. Dev. = standard deviation.

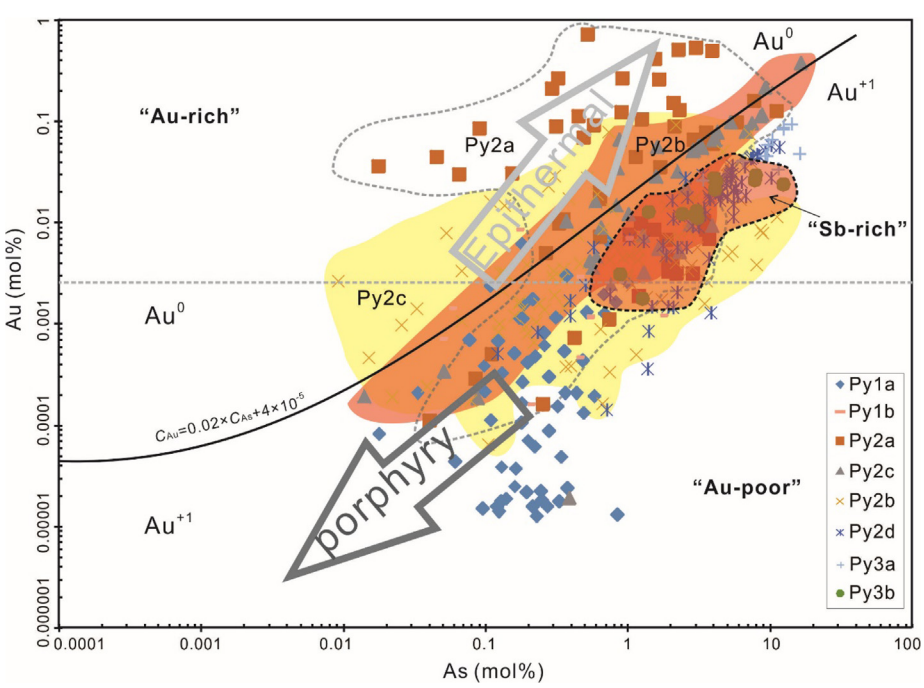

Fig. 7. Plot of Au *vs.* As for pyrite. The solubility limit for gold is approximated by the line $C_{Au} = 0.02*C_{As} + 4*10^{-5}$, where C_{Au} and C_{As} represent the concentrations of Au and As in mol.% (Reich et al., 2005). Below this line, Au is present in solid solution (Au^{+1}), whereas above it a significant amount of Au is contained as nanoparticles of native Au (Au^0). "Au-rich" represents pyrite with > 2 ppm Au, and "Au-poor" represents pyrite with < 2 ppm Au. "Sb-rich" represents pyrite from Stage-3. The porphyry arrow represents porphyry-related pyrite (low Au and As); the 'epithermal' arrow represents epithermal pyrite (higher Au and As). Py-pyrite, Ccp-chalcopyrite, Sph-sphalerite.

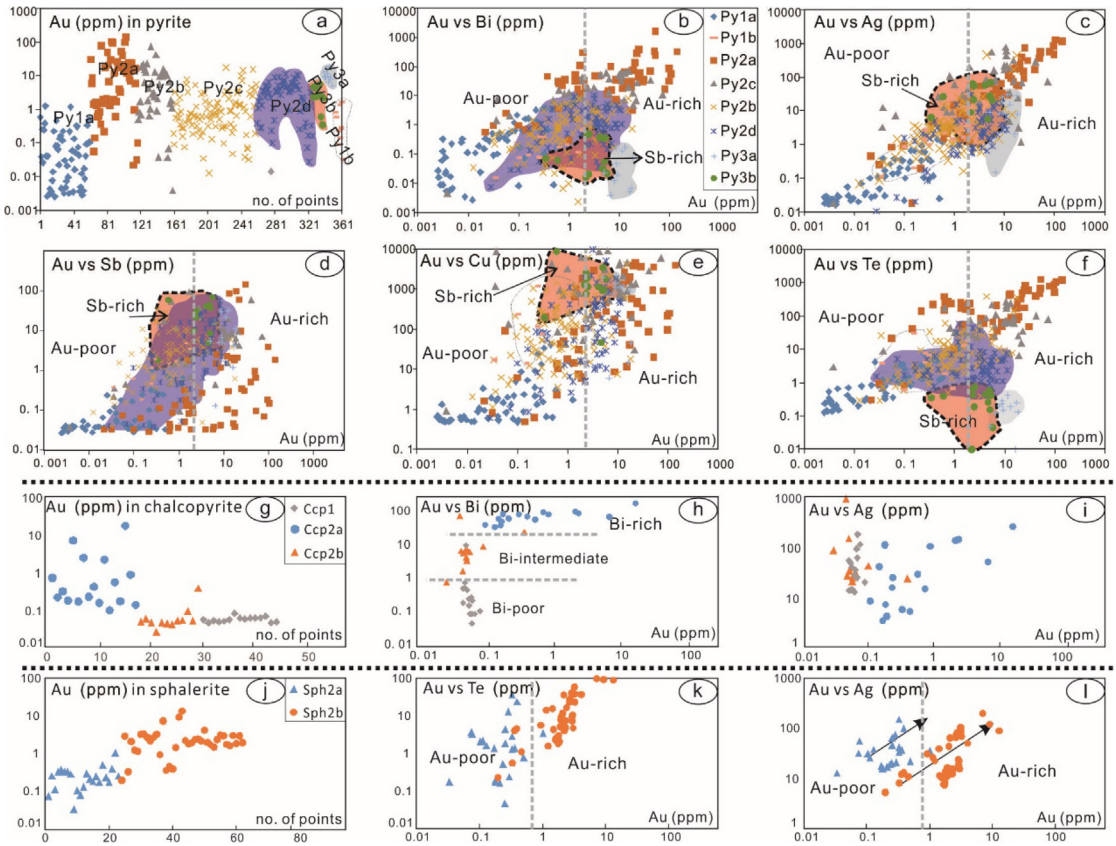

Fig. 8. Diagrams illustrating variation in the concentrations of Au and selected trace elements (in ppm) for pyrite, sphalerite and chalcopyrite. a) Au contents in pyrite. b) Binary plot of Au *vs.* Bi in pyrite showing a positive correlation (except for Sb-rich pyrite) and a clear discrimination between the three groups. c) Binary plot of Au *vs.* Ag in pyrite showing a positive correlation. The three pyrite groups are also well discriminated on this plot. d) Binary plot of Au *vs.* Sb in pyrite showing a similar positive correlation and discrimination between the three groups of pyrites. e) Binary plot of Au *vs.* Cu in pyrite showing a positive correlation. f) Binary plot of Au *vs.* Te for pyrite showing a positive correlation. Metamorphic pyrite (Py3b, Sb-rich pyrite) does not show the same positive correlation. g) Au contents in chalcopyrite. h) Binary plot of Au *vs.* Bi in chalcopyrite showing no systematic positive correlation. Three groups of chalcopyrite can be recognized based on the variation in Sb content. i) Binary plot of Au *vs.* Ag in chalcopyrite showing a weak positive correlation. j) Au contents in sphalerite. k) Binary plot of Au *vs.* Te in sphalerite. No clear positive correlation is visible. The two group of sphalerite plot distinctly based on the difference in Au content. l) Binary plot of Au *vs.* Ag in sphalerite showing a positive correlation. Py-pyrite, Ccp-chalcopyrite, Sph-sphalerite.

from porphyry systems elsewhere (Reich et al., 2013b; George et al., 2016), with the lowest Au concentrations (mostly below the minimum detection limit), 13.5–191 ppm Ag (mean 53.0 ppm), and 0.54–3.4 ppm Te (mean 2.2 ppm) (Table 3).

4.2.3. Sphalerite

Trace element concentrations in sphalerite were measured in three samples (62 spot analyses). Two groups are identified based on their trace element signatures: a Au-poor group; and a Au-rich group. Gold-poor sphalerite (mean 0.27 ppm) coexists with chalcopyrite whereas Au-rich sphalerite (mean 2.6 ppm) does not. The Au-poor group contains lesser Te (4.5 ppm), Sb (3.2 ppm), and As (1.3 ppm) but is comparatively higher in Bi (mean 13.3 ppm), Hg (42.4 ppm), Pb (733 ppm), and Cu (1052 ppm) (Electronic Appendix 1). The Au-rich group contains higher Te (18.5 ppm), Sb (4.6 ppm), and As (7.4 ppm), and lower Bi (mean 0.77 ppm), Hg (29 ppm), Pb (66 ppm), and Cu (92 ppm) (Table 3, Supplement 3). Fig. 8k and l illustrate the positive Au-Te and Au-Ag correlations in sphalerite.

5. Discussion

The distributions of gold and other trace elements in sulfide minerals precipitated from hydrothermal solutions can be used to infer changes in the physicochemical conditions during mineralization, and also, potentially, establish genetic links between porphyry systems and associated epithermal environments (e.g., Hedenquist and Lowenstern, 1994; Large et al., 2009; Reich et al., 2013a; Deditius et al., 2014; Zwahlen et al., 2014). Pyrite, sphalerite, and chalcopyrite are the most abundant sulfide minerals in the Zhengguang deposit and occur in all parts of the mineralization. Recognition of distinct Au-poor, Au-rich, and Sb-rich populations of pyrite, distinct types of chalcopyrite distinguished by Bi content, and two types of sphalerite, thus provides an opportunity to place constraints on ore genesis and the evolution of mineralizing processes in an intermediate sulfidation epithermal deposit. Based on observation of mineral assemblages and textures, and trace element datasets for each sulfide, we discuss how these data can help define relationships between porphyry- and epithermal-style mineralization.

5.1. Inferences for a potential porphyry system

5.1.1. Pyrite chemistry

Pyrite is a refractory mineral that may contain measurable concentrations of Au, Ag, Cu, Pb, Zn, Co, Ni, As, Sb, Se, Te, Hg, Tl, and Bi. Pyrite mineral chemistry can provide valuable information to assist understanding the genesis of mineral deposits (e.g., Large et al., 2009; Reich et al., 2013a). Pyrite is also an important gold carrier and may be the dominant host in some gold deposits (e.g., Cook and Chryssoulis, 1990; Deditius et al., 2011). Trace metals such as Au, Ag, and Sb are very commonly enriched in arsenian pyrite (e.g., Hannington et al.,

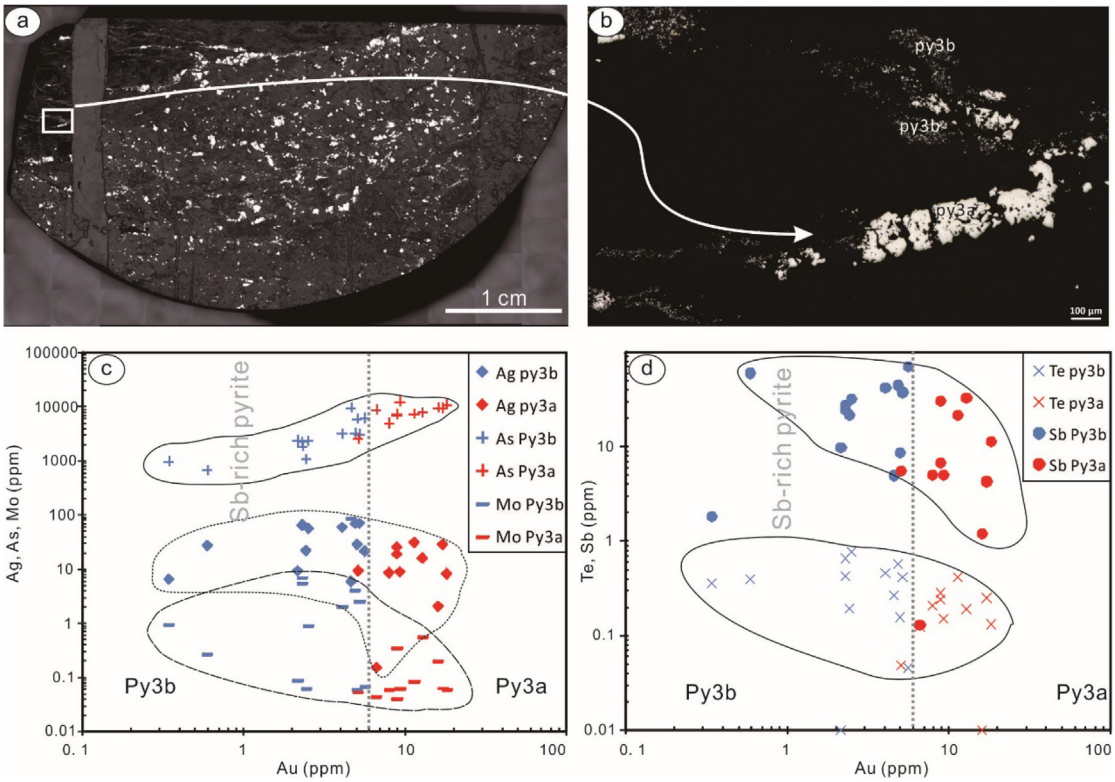

Fig. 9. a) Reflected light photomicrograph of metamorphosed ore and b) metamorphic (recrystallized) pyrite. c) Binary plots of Au *vs.* Ag, As, and Mo. Note positive correlations between Au and Ag, and Mo, and the negative correlation between Au and Cu in Py3a and Py3b. d) Binary plots of Au *vs.* Te, and Sb. Note the positive correlations between Au and Te, and Sb. Py-pyrite.

1991; Reich et al., 2005). In Carlin-type gold deposits of Nevada, the second largest gold concentration on Earth, gold concentrations may be up to 10,000 ppm in arsenian pyrite (e.g., Cline et al., 2005; Muntean et al., 2011). Prior research has thus focused on the relationship between As and Au in As-rich pyrite (e.g., Reich et al., 2013a). "Invisible" gold in As-rich pyrite is represented either by sub-microscopic inclusions of Au minerals (native gold, sometimes compounds of Au with Te, more rarely with Sb, Bi, As, Se, Sn, and Hg), or by Au substituted directly into the crystal lattice (e.g., Fleet and Mumin, 1997; Simon et al., 1999; Vaughan and Kyin, 2004; Tauson et al., 2014). Reich et al. (2005) showed that As-rich pyrite incorporates invisible gold in direct proportion to the As content. The maximum amount of solid solution Au in arsenian pyrite was defined as $C_{Au} = 0.02 \times C_{As} + 4 \times 10^{-5}$, where C_{Au} and C_{As} are the mol% concentrations of Au and As, respectively (Fig. 7). These authors considered that arsenian pyrite plotting above this line infers the presence of nanoparticulate Au (Au^0), whereas those plotting below the line contain solid solution Au (Au^{+1}).

Pyrite geochemistry in representative samples from Zhengguang indicates a wide variation of Au concentration, defining three groups (Au-poor, Au-rich, and Sb-rich; Table 3). Au-As relationships in pyrite from porphyry and epithermal deposits are shown in Fig. 7 (Reich et al., 2013a; Deditius et al., 2014). From this diagram, the solubility limit of Au as a function of As separates the Zhengguang pyrites into two fields: sub-populations of Py2a, Py2b, Py2c groups lie above the inferred solubility limit, while the Au-poor group (Py1a, Py1b and a part of the Py2a, Py2b, Py2c, Py2d populations) plot below the solubility limit, close to the porphyry field (Deditius et al., 2014). According to the function of Reich et al. (2005), Au occurs as structurally-bound ions (Au^{1+}) in solid solution in the Au-poor pyrite group from Zhengguang. Among the Au-poor group of pyrite, Au nevertheless shows positive correlations with Bi, Te, Ag and Cu (Fig. 8b-f), potentially indicating the presence of sub-microscopic Au-Ag-Te minerals, (Ag)-Bi-Pb-sulfosalts, or Bi-tellurides/tellurosulfides (Zhang et al., 2014; Mills et al., 2015).

Although classified as an intermediate sulfidation epithermal deposit, Zhengguang is considered as part of a larger magmatic-hydrothermal porphyry-epithermal Cu-Mo-Au system based on a detailed comparison between the Zhengguang epithermal deposit and Duobaoshan-Tongshan porphyry deposits (Song et al., 2015). Until now, however, there is no unequivocal evidence to validate such a hypothesis. Because Au-poor pyrite (Py1a, Py1b) contains extremely low concentrations of gold and related trace elements (Fig. 7; Table 3), and thus resembles pyrite from porphyry-type mineralization (e.g., Reich et al., 2013a; Zwahlen et al., 2014), it is tempting to infer a relationship with a porphyry system. Both mineral morphology and geochemistry may reveal connections between porphyry and epithermal mineralization (e.g., Deditius et al., 2009, 2014; Maydagán et al., 2013; Zwahlen et al., 2014). In general, pyrite crystals from the porphyry stage are fine-grained (0.04–0.5 mm), trace element-poor (Franchini et al., 2015), and contain low concentrations of Au (mostly < 2 ppm), As (< 1000 ppm), Te (< 10 ppm) and Ag (< 10 ppm) (e.g., Gregory et al., 2013; Maydagán et al., 2013; Franchini et al., 2015). Low-temperature pyrite tends to contain more As (and hence, Au) in solid solution, whereas higher temperature pyrite contains less As and hosts Au as particles, a change that occurs at ~300 °C (Maddox et al., 1998; Pokrovski et al., 2002; Reich and Becker, 2006). Previous studies have proposed that Au may be scavenged from porphyry Cu systems by high-temperature (600–700 °C) vapor phases (Kesler et al., 2002), resulting in a relative depletion of gold in minerals from the porphyry system (Franchini et al., 2015). The results of Reich et al. (2013a), in their study of the Dexing porphyry Cu-(Mo-Au) deposit, China, show that most porphyry-type pyrite plots below the solubility line defined by Reich et al. (2005). Therefore, we consider that the Au-poor group of pyrite from Zhengguang, which are characterized by low concentrations of Au and related trace elements, belong to a porphyry-related mineralization system (Fig. 10b). Both samples containing Au-poor pyrites (49275-2-1235 and 58-8-616) were

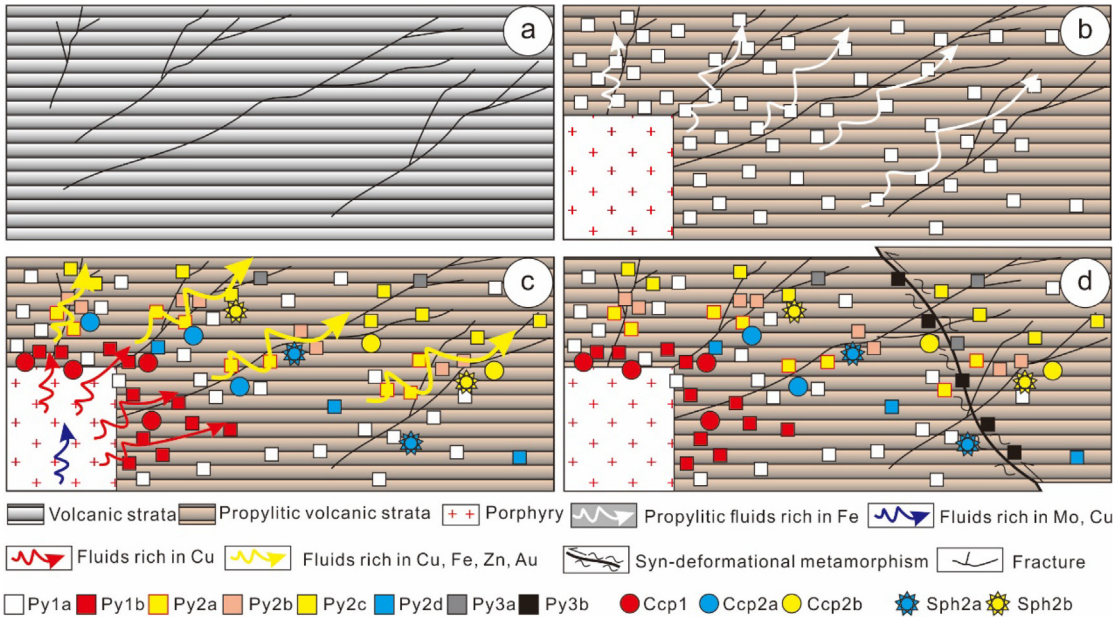

Fig. 10. Mineralization model for the Zhengguang epithermal gold deposit based on results of sulfide petrography and geochemistry. a) Emplacement of volcanic rocks and development of structures. b) Pyrite zone developed during porphyry emplacement and formation of first-stage pyrite (Py1a). c) Early porphyry pyrite is altered and overprinted by high-temperature, porphyry-related Cu-rich fluids (Py1b, Ccp1) and subsequently by lower-temperature epithermal fluids (Py2a, Py2b, Py2c, Py2d, Sph1, Sph2b, Ccp2a, and Ccp2b). d) Deformation and alteration of epithermal sulfides during a superimposed metamorphic event, leading to formation of Py3a and Py3b. Py-pyrite, Ccp-chalcopyrite, Sph-sphalerite.

collected from drillholes intersecting veins at depth, far from the main zone of epithermal mineralization, and are entirely enclosed by rocks affected by propylitic alteration (Fig. 2b). We interpret the Au-poor group of pyrite to have formed within a zone of pyritization associated with emplacement of the porphyry rocks (Seedorff et al., 2005; Liu et al., 2016; see Fig. 10b). Some data from other pyrite from Zhengguang provides additional support for this interpretation. A portion of data from the Py2a, Py2b, Py2c, Py2d sub-types also show low concentrations of Au and related trace elements. They are likely relicts of porphyry-related pyrite preserved after partial replacement by later epithermal Au-bearing fluids (Fig. 4b, d, j, k, p), analogous to those described by Franchini et al. (2015).

Copper concentrations in Au-poor pyrite lend additional support to this hypothesis. The Cu concentration in Au-poor pyrite from Zhengguang can be as high as 10,000 ppm (Fig. 7e; Supplement 1–3), significantly higher than in most gold deposits (e.g., Mills et al., 2015; Zhao et al., 2016). Although it is commonly accepted that most Cu occurs in pyrite as inclusions of Cu-sulfides (e.g., chalcopyrite), evidence has also been reported to show that Cu can be accommodated within the pyrite structure, in some cases reaching wt% levels (e.g., Pacevski et al., 2008). High Cu contents in pyrite and a positive correlation between Au and Cu can indicate a porphyry Cu system in the region, as suggested by Reich et al. (2013a) from Dexing, where pyrite may contain > 6 wt% Cu. The high Cu content and positive correlation with Au in Au-poor pyrite is thus taken to indicate a porphyry Cu system in the region, in accord with the distribution of ore deposits in the Duobaoshan orefield (Song et al., 2015).

5.1.2. Chalcopyrite geochemistry

Studies addressing trace element concentrations in chalcopyrite are relatively scarce compared to other common sulfides such as pyrite, sphalerite, or galena. Much of the published data for chalcopyrite (e.g., Moggi-Cecchi et al., 2002; Shalaby et al., 2004) focused on a limited suite of trace elements. An overview of the trace element chemistry of chalcopyrite from different ore deposits was, however, presented by George et al. (2018). They showed that chalcopyrite can, in some cases, host a wide range of trace elements, including Mn, Co, Zn, Ga, Se, Ag, Cd, In, Sn, Sb, Hg, Tl, Pb and Bi, but that chalcopyrite is always very poor in Au. This supports previous work showing that chalcopyrite may contain up to a few ppm Au at most (e.g., Vikentyev et al., 2004). Simon et al. (2000) showed that up to 16 ppm Au is soluble in chalcopyrite at 500 °C, dropping to 4 ppm at 400 °C. Reich et al. (2013a) document up to 1.66 ppm Au in chalcopyrite from the Mantos Blancos deposit, Chile. Chalcopyrite crystallizing in the absence of sphalerite and/or galena is likely to host greater concentrations of Bi. Bismuth will be preferentially incorporated into galena whenever the three minerals co-crystallize (George et al., 2016).

Based on Bi concentration, three groups of chalcopyrite are recognized from Zhengguang (Fig. 8g-i). Among these, the Bi-poor group (Ccp1) are similar to chalcopyrite from porphyry systems (e.g., Reich et al., 2013b; George et al., 2018) in that they have low concentrations of Au, Ag, Te, As, the least Bi and most Mo. Porphyry-type chalcopyrite contains low concentration of Ag and high concentrations of Zn, while epithermal chalcopyrite has a high concentration of Ag (George et al., 2018).

5.2. Sulfide-hosted gold in epithermal systems

5.2.1. Au-bearing pyrite

In all epithermal sulfide-bearing veins from Zhengguang, early, euhedral, coarse-grained pyrite is overprinted and replaced by later base metal sulfide mineralization (sphalerite, galena, chalcopyrite, etc.) accompanied by deposition of precious metals (Figs. 4–6). Published research shows that low-temperature epithermal fluids, typically rich in base and precious metals, gradually evolve from high-temperature magmatic fluids, which are characteristically enriched in elements such as Mo and Cu concentrated within or immediately adjacent to the porphyry system (e.g., Heinrich, 2005; Kovalenker et al., 2006; Gu et al., 2016).

To understand the genesis of epithermal ore deposits, researchers have focused on the chemistry of minerals deposited from hydrothermal fluids, including alunite, adularia, pyrite, sphalerite, chalcopyrite, and galena (e.g., Kouzmanov et al., 2002; Bendezu et al., 2008; Voudouris, 2014; Liu et al., 2016). Epithermal pyrite contains relatively

high concentration of Au (typically > 8 ppm, up to 3.41 wt%), As (> 1000 ppm, up to a few wt.%), Te (> 10 ppm) and Ag (up to a few wt %) (e.g., Deditius et al., 2009, 2014; Maydagán et al., 2013; Reich et al., 2013a; Zwahlen et al., 2014; Franchini et al., 2015). Trace element signatures of relatively Au-rich pyrites from Zhengguang are consistent with those of epithermal pyrite. These replace porphyry-related pyrite and contain elevated concentrations of Au (mostly > 8 ppm and up to 140 ppm). Epithermal pyrite contains gold in two forms: in solid solution as Au^{1+}; and as micro- to nano-sized inclusions as Au^0 (Reich et al., 2013a) (Fig. 7). This indicates that after formation of Au-poor pyrite, later epithermal fluids overprinted and replaced early pyrite, forming a new generation of Au-rich pyrite (Fig. 10c).

Arsenic contents in pyrite vary from ~10 up to ~10,000 ppm; most in the Au-rich pyrite are > 500 ppm. Our results show that significant Au content (8–140 ppm) is always associated with high As (> 500 ppm) in pyrite types Py2a, Py2b, Py2c, and Py2d (Fig. 8, b-d; Table 2). The distribution of points for Py2a, Py2b, and Py2c on Fig. 7 indicates that Au-rich pyrite, coexisting with epithermal chalcopyrite and sphalerite, contains Au as both Au^0 and Au^{+1}. Research on pyrite from Carlin-type and epithermal deposits show similar features, the solutions forming epithermal deposits were largely saturated with respect to Au, whereas those forming Carlin-type deposits were largely undersaturated and that solid-solution Au was probably removed from fluids by adsorption (Reich et al., 2005). On the basis that Py2a, Py2b, and Py2c have saturated and undersaturated Au in the same sample, we can propose that Cu-Zn-Fe-Au-bearing ore-forming fluids altered and replaced pre-existing pyrite. This is fully concordant with observations showing abundant inclusions of native gold and electrum in Py2a, Py2b, and Py2c (Fig. 4, b-p).

5.2.2. Constraints from chalcopyrite chemistry

Trace element data for chalcopyrite further support the above discussion. Although chalcopyrite contains far less Au than pyrite, there are nevertheless significant differences between the three groups. Epithermal Bi-rich chalcopyrite (Ccp2a), which replaces Py2a, also contains the most Au (2 ppm) and Te, and the least Sb. The Bi-poor group of chalcopyrite (Ccp1), formed in the porphyry environment and contains the least gold (mean 0.06 ppm). The chemistry of the intermediate- and high-Bi chalcopyrite resembles that from epithermal systems (Reich et al., 2013b; George et al., 2018).

All three chalcopyrite sub-types contain relatively high contents of Ag (up to 1000 ppm), which displays no correlation with Au (Fig. 8i). These differences indicate that although chalcopyrite is a poor host for Au, the mineral can readily incorporate Ag, particularly when bornite and chalcocite are absent (George et al., 2018).

5.2.3. Constraints from sphalerite chemistry

After pyrite, sphalerite is the second most abundant sulfide in the Zhengguang deposit. Results show that Au-poor sphalerite (Sph2a) contains less Au, Te, and more Cu (up to 3902 ppm) than Au-rich sphalerite (Sph2b) (up to 13.2 ppm Au (Supplement 1). Both groups formed in the epithermal environment via replacement of pre-existing sulfides. Sphalerite has been proposed as a suitable carrier for gold (Dai et al., 2011), and is often closely related with gold mineralization (Vikentyev et al., 2004; Radosavljevic et al., 2016). Cook et al. (2009) used LA-ICP-MS to investigate the distribution of trace elements in sphalerite from 26 ore deposits. They found that Cd, Co, Ga, Ge, In, Mn, Sn, As and Tl occur in solid solution within sphalerite, and that sphalerite can also incorporate minor amounts of As, Se, and possibly also Au. Variations in Cu concentration in sphalerite are, however, commonly due to variation in the density of chalcopyrite inclusions rather than lattice-bound Cu (Lockington et al., 2014). In the case of ores from Uzelginsk, Russia, sphalerite commonly contains 1.5–4.5 ppm Au, with higher Au contents (1.8–10.6 ppm) coincident with emulsion-like inclusions of chalcopyrite (Vikentyev et al., 2004). These tiny inclusions of gold-bearing chalcopyrite in sphalerite were considered to account for most of the gold. In our study, sphalerite which coexists with epithermal chalcopyrite (Figs. 4c and 5c), is Au-poor and sphalerite without co-existing chalcopyrite (Figs. 4d and 6d–e), contains the highest Au concentration (Supplement 3). This emphasizes the critical importance of equilibrium partitioning between co-crystallizing sulphides (George et al., 2016). Additionally, microscopic observation shows abundant inclusions of native gold within Sph2a and Sph2b (Fig. 6c–d). These results are consistent with Cabri et al. (2000), who found that gold inclusions are most abundant in sphalerite with low As content from ultramafic-hosted hydrothermal systems. Summarising the above, sphalerite is a minor Au-carrier in the Zhengguang deposit. Coexistence with epithermal chalcopyrite will, however, lead to a preferential partitioning of Au into the latter.

Relationships between Au and Te, Ag, As, Fe, Cu in sphalerite are of interest for understanding orebody evolution. Plots of Au *vs.* Te, Au *vs.* Ag, Au *vs.* Fe, and Au *vs.* Cu (Fig. 8j–l) all show positive correlations. Cook et al. (2009) and Ciobanu et al. (2011) found that Ag can exist as microscopic Ag-bearing mineral inclusions in sphalerite, as well as substituted in the lattice (as Ag^{1+}). Because of the strong positive correlation between Au and Ag, we believe that Au may also potentially occur as Au^{1+} or Au-bearing mineral inclusions in sphalerite. Correlations between Au and Te, Ag, As, Fe and Cu may reflect this dual character (Fig. 8j–l).

Iron content in sphalerite is used as an indicator of the sulfidation state of gold mineralization in VMS systems (Hannington and Scott, 1989). These authors considered a negative correlation between the average FeS content of sphalerite from some VHMS deposits and the gold grades of those deposits (Ramsden et al., 1991; Herzig and Hannington, 1993). This hypothesis is supported by data from Uralian VMS deposits (Vikentyev et al., 2004; Vikentyev, 2006), showing that the concentration of Au in minerals increases with a decrease in the Fe-content of coexisting sphalerite. The work reported here shows a contrasting relationship between Au and Fe, more analogous to the phenomenon reported by Zaw and Large (1996) who determined that the complex relationship between mol.% FeS in sphalerite and gold grades in Tasmanian VMS deposits is a function of the redistribution of FeS in sphalerite during a superimposed Devonian metamorphic and metasomatic event.

5.3. Pyrite metamorphism

Sample 49275-2-78 from Zhengguang contains two types of pyrite: an epithermal type displaying a slight metamorphic overprint; and a more strongly altered type (Fig. 4g). These observations indicate that subsequent to deposition, the Zhengguang deposit underwent a period of compressive deformation and metamorphism (Figs. 9 and 10d). This provides an opportunity to address gold behavior during this overprinting event.

Metamorphism in the Duobaoshan orefield has been discussed in several studies (Du et al., 1988; Wang et al., 2007; Pang et al., 2017). After deposit formation in the Paleozoic, tectonic-magmatic activity during the Hercynian and Yanshanian orogenies impacted on the Cu-Mo-Au ores (Pang et al., 2017). NW-striking faults and deformation dominate the tectonic pattern in Zhengguang Paleozoic volcanic sedimentary rocks (Song et al., 2015). This feature is recognized in sample 49275-2-78 with a clearly-oriented structure that deforms pre-existing Au-bearing quartz-polymetallic sulfides veins (Fig. 9a-b). Research focused on orogenic gold mineralization at Kalgoorlie, Western Australia indicates that it formed in an epigenetic setting as a result of orogenic processes, without significant direct involvement of magmatic fluids. Mineralizing fluids were instead sourced from greenstone lithologies during regional metamorphism (e.g. Phillips and Powell, 2010; Vielreicher et al., 2016). Other researchers have focused on the behavior of gold associated with metamorphosed pyrite (e.g., Larocque and Hodgson, 1995; Craig et al., 1998; Clark et al., 2004; Deol et al., 2012; Zhang et al., 2014; Mills et al., 2015; Zhao et al., 2016). Metamorphic

recrystallization results in a release of invisible gold from pyrite and may be an important process in upgrading refractory gold in pyrite to a more easily recoverable form (electrum) (Larocque and Hodgson, 1995; Larocque et al., 1995). Chemical mapping of pyrite, including examples from ores metamorphosed at amphibolite facies or higher, reveals that the pyrite may nevertheless retain physical and chemical textures allowing interpretation of both the depositional and the post-depositional history of the deposit (Cox, 1987; Cook et al., 1994; Clark et al., 2004).

LA-ICP-MS analysis of the two pyrite generations from Zhengguang indicates that recrystallized Py3b is relatively depleted in Au, As and Te and relatively enriched in Sb, Ag, Cu and Mo (Table 3; Fig. 9). Coexisting epithermal Py3a is, in contrast, relatively rich in Au and As and poor in Sb, Ag, Cu, and Mo (Fig. 9). We interpret these differences in terms of post-formation metamorphic overprinting, in which Au, As, and Sb were remobilized from epithermal pyrite (Fig. 10d), whereas Sb, Ag, Cu, and Mo are incorporated into the new recrystallized pyrite. Plots of Au *vs.* Ag, Mo, As, Te, Sb, show negative correlations between Au and Ag, Mo, Te, Sb, and a positive correlation between Au and As (Fig. 9). This is concordant with Larocque and Hodgson (1995) who found that recrystallized pyrite contains less Au than associated primary pyrite, and that syn-deformational recrystallization results in the release of gold (Huston et al., 1995).

6. Conclusions

Based on BSE imaging and LA-ICP-MS analysis, the textures and Au distributions are described in pyrite, sphalerite and chalcopyrite from the Zhengguang gold deposit. Pyrite formed throughout ore deposit evolution from early porphyry-style mineralization to subsequent epithermal-type mineralization, and also during the latest metamorphic event that overprints the ores. The Au concentrations of various subgroups of pyrite, sphalerite and chalcopyrite were constrained and compared to literature data for the same minerals in typical porphyry-epithermal deposits.

Emplacement of the porphyry results in the formation of Au-poor pyrite and Bi-poor chalcopyrite. Later epithermal fluids alter and overprint early pyrite resulting in deposition of gold and base metal sulfides, including Au-rich pyrite, Bi-rich chalcopyrite, and Au-rich sphalerite. Gold is most likely derived from magma-derived fluids. Gold occurs as Au^{1+} in the Au-poor and Sb-rich pyrite sub-groups, and as Au^{1+} and Au^{0} in Au-rich pyrite. Among the sulfides, pyrite is the most important gold carrier. Sphalerite is a minor Au-host but coexistence with epithermal chalcopyrite leads to a decrease in the Au content of sphalerite. Chalcopyrite is not a good host for gold, but a good host for silver. A metamorphic event impacted on early-formed sulfides, resulting in a deformation overprint and associated Au remobilization.

Acknowledgements

This study was supported byNational Natural Science Foundation of China (grant No. 41572064 and No. 41390444). All analytical work was carried out while the first author was a visiting scholar at the University of Adelaide. We would like to thank Jihai Guo, Haijun Liang, Kuangyin Tong, Hui Tang, Xuyong Pang, Chao Zhao for their kind support during fieldwork. Insightful comments from Panos Voudouris, an anonymous reviewer, and Editor-in-Chief Franco Pirajno are highly appreciated. We also express our appreciation to Benjamin Wade, Aoife McFadden, Ken Neubauer, Zhiyong Zhu, and Wenyuan Gao for their support with analysis.

Appendix A. Supplementary data

Supplementary data to this article can be found online at https://doi.org/10.1016/j.oregeorev.2019.02.001.

References

Bendezu, R., Page, L., Spikings, R., Pecskay, Z., Fontbote, L., 2008. New Ar-40/Ar-39 alunite ages from the Colquijirca district, Peru: evidence of a long period of magmatic SO_2 degassing during formation of epithermal Au-Ag and Cordilleran polymetallic ores. Mineral. Deposita 43, 777–789.
Buslov, M., Watanabe, T., Saphonova, I.Y., Iwata, K., Travin, A., Akiyama, M., 2002. A Vendian-Cambrian island arc system of the Siberian continent in Gorny Altai (Russia, Central Asia). Gondwana Res. 5, 781–800.
Cabri, L.J., Newville, M., Gordon, R.A., Crozier, E.D., Sutton, S.R., McMahon, G., Jiang, D.-T., 2000. Chemical speciation of gold in arsenopyrite. Can. Mineral. 38, 1265–1281.
Ciobanu, C.L., Cook, N.J., Utsunomiya, S., Pring, A., Green, L., 2011. Focussed ion beam–transmission electron microscopy applications in ore mineralogy: bridging micro-and nanoscale observations. Ore Geol. Rev. 42, 6–31.
Clark, C., Grguric, B., Schmidt Mumm, A., 2004. Genetic implications of pyrite chemistry from the Palaeoproterozoic Olary Domain and overlying Neoproterozoic Adelaidean sequences, northeastern South Australia. Ore Geol. Rev. 25, 237–257.
Cline, J.S., Hofstra, A.H., Muntean, J.L., Tosdal, R.M., Hickey, K.A., 2005. Carlin-type gold deposits in Nevada: Critical geologic characteristics and viable models. Economic Geology 100th Anniversary Volume, pp. 451–484.
Cook, N.J., Chryssoulis, S.L., 1990. Concentrations of invisible gold in the common sulfides. Can. Mineral. 28, 1–16.
Cook, N.J., Klemd, R., Okrusch, M., 1994. Sulphide mineralogy, metamorphism and deformation in the Matchless massive sulphide deposit, Namibia. Mineral. Deposita 29, 1–15.
Cook, N.J., Ciobanu, C.L., Pring, A., Skinner, W., Shimizu, M., Danyushevsky, L., Saini-Eidukat, B., Melcher, F., 2009. Trace and minor elements in sphalerite: a LA-ICPMS study. Geochim. Cosmochim. Acta 73, 4761–4791.
Cox, S., 1987. Flow mechanisms in sulphide minerals. Ore Geol. Rev. 2, 133–171.
Craig, J., Vokes, F., Solberg, T., 1998. Pyrite: physical and chemical textures. Mineral. Deposita 34, 82–101.
Cui, G., Wang, J.Y., Zhang, J.X., Cui, G., 2008. U-Pb SHRIMP dating of zircons from Duobaoshan granodiorite in Heilongjiang and its geological significance. Global Geol. 27 (4), 387–394 (in Chinese with English abstract).
Dai, H.Z., Chen, C.H., Gu, X.X., Dong, S.Y., 2011. Typomorphic characteristics of pyrite, arsenopyrite, sphalerite from Zhesang gold deposit in Funing County of Yunnan province. Acta Mineral. Sin. S1, 194–195 (in Chinese with English abstract).
Deditius, A.P., Utsunomiya, S., Kesler, S.E., Ewing, R.C., Walshe, J., 2009. August. Behaviour of trace elements in arsenian pyrite in ore deposits. Proceedings Tenth Biennial SGA Meeting of the Society for Geology Applied to Mineral Deposits, Townsville, Queensland, Australia, 2009. 710–712.
Deditius, A.P., Utsunomiya, S., Reich, M., Kesler, S.E., Ewing, R.C., Hough, R., Walshe, J., 2011. Trace metal nanoparticles in pyrite. Ore Geol. Rev. 42, 32–46.
Deditius, A.P., Reich, M., Kesler, S.E., Utsunomiya, S., Chryssoulis, S.L., Walshe, J., Ewing, R.C., 2014. The coupled geochemistry of Au and As in pyrite from hydrothermal ore deposits. Geochim. Cosmochim. Acta 140, 644–670.
Deng, J., Wang, Q.F., 2016. Gold mineralization in China: metallogenic provinces, deposit types and tectonic framework. Gondwana Res. 36, 219–274.
Deng, K., Li, N., Yang, Y.F., Zhang, C., Yu, Y.B., Zhang, D.C., 2013. Fluid inclusion constraints on the origin of the Zhengguang gold deposit, Heihe City, Heilongjiang Province. Acta Petrol. Sin. 29, 231–240 (in Chinese with English abstract).
Deol, S., Deb, M., Large, R.R., Gilbert, S., 2012. LA-ICPMS and EPMA studies of pyrite, arsenopyrite and loellingite from the Bhukia-Jagpura gold prospect, southern Rajasthan, India: Implications for ore genesis and gold remobilization. Chem. Geol. 326, 72–87.
Du, Q., Zhao, Y.M., Lu, B.G., Ma, D.Y., Li, P.L., Lv, J.K., Li, W.S., Ao, L.Z., Cui, G., 1988. The Duobaoshan Porphyry Copper Deposit. Geological Publishing House, Beijing 1–155 (in Chinese).
Einaudi, M.T., Hedenquist, J.W., Inan, E., 2003. Sulfidation state of hydrothermal fluids: The porphyry-epithermal transition and beyond. Society of Economic Geologists and Geochemical Society Special Publication 10, 285–313.
Fleet, M.E., Mumin, A.H., 1997. Gold-bearing arsenian pyrite and marcasite and arsenopyrite from Carlin Trend gold deposits and laboratory synthesis. Am. Mineral. 82, 182–193.
Franchini, M., McFarlane, C., Maydagan, L., Reich, M., Lentz, D.R., Meinert, L., Bouhier, V., 2015. Trace metals in pyrite and marcasite from the Agua Rica porphyry-high sulfidation epithermal deposit, Catamarca, Argentina: textural features and metal zoning at the porphyry to epithermal transition. Ore Geol. Rev. 66, 366–387.
Fu, Y.L., Yang, Y.C., 2010. Deposit genesis and prospecting criteria of Zhengguang gold deposit, Heilongjiang. Gold 8 (in Chinese with English abstract).
Gao, R., Lü, X., Yang, Y., Li, C., 2014. Characteristics of cryptoexplosive breccias in the Zhengguang gold deposit of Heilongjiang Province and their geological implications. Geol. Explor. 50, 874–883.
George, L.L., Cook, N.J., Ciobanu, C.L., 2016. Partitioning of trace elements in co-crystallized sphalerite–galena–chalcopyrite hydrothermal ores. Ore Geol. Rev. 77, 97–116.
George, L.L., Cook, N.J., Crowe, B.B.P., Ciobanu, C.L., 2018. Trace elements in hydrothermal chalcopyrite. Mineral. Mag. 82, 59–88.
Goldfarb, R.J., Taylor, R.D., Collins, G.S., Goryachev, N.A., Orlandini, O.F., 2014. Phanerozoic continental growth and gold metallogeny of Asia. Gondwana Res. 25, 48–102.
Gregory, M.J., Lang, J.R., Gilbert, S., Hoal, K.O., 2013. Geometallurgy of the Pebble porphyry copper-gold-molybdenum deposit, Alaska: implications for gold distribution and paragenesis. Econ. Geol. 108, 463–482.

Gu, A.L., Men, L.J., Sun, J.G., Nagao, K., Bai, L.A., Cui, L.P., Chai, P., Chen, Y.J., Zhu, J.Q., 2016. Origin and evolution of ore fluids in the late Mesozoic Naozhi epithermal Au-Cu deposit, Yanbian area, Northeast China: evidence from fluid inclusion and isotopic geochemistry. Arabian J. Geosci. 9, 117.
Han, C.M., Xiao, W.J., Zhao, G.C., Mao, J.W., Li, S.Z., Yan, Z., Mao, Q.G., 2006. Major types, characteristics and geodynamic mechanism of Upper Paleozoic copper deposits in northern Xinjiang, northwestern China. Ore Geol. Rev. 28, 308–328.
Han, C.M., Wang, C.S., Li, Z.M., 2007. Duobaoshan Copper's Resource and Potential. Geological Publishing House, Beijing, pp. 1–68 (in Chinese with English abstract).
Hannington, M.D., Herzig, P., Scott, S., Thompson, G., Rona, P., 1991. Comparative mineralogy and geochemistry of gold-bearing sulfide deposits on the mid-ocean ridges. Mar. Geol. 101, 217–248.
Hannington, M.D., Scott, S.D., 1989. Sulfidation equilibria as guides to gold mineralization in volcanogenic massive sulfides; evidence from sulfide mineralogy and the composition of sphalerite. Econ. Geol. 84, 1978–1995.
Hao, Y.J., Ren, Y.S., Duan, M.X., Tong, K.Y., Chen, C., Yang, Q., Li, C., 2015. Metallogenic events and tectonic setting of the Duobaoshan ore field in Heilongjiang Province. NE China. J. Asian Earth Sci. 97, 442–458.
Hedenquist, J.W., Lowenstern, J.B., 1994. The role of magmas in the formation of hydrothermal ore deposits. Nature 370, 519–527.
Hedenquist, J.W., Arribas, A., Gonzalez-Urien, E., 2000. Exploration for epithermal gold deposits. Rev. Econ. Geol. 13, 245–277.
Heinrich, C.A., 2005. The physical and chemical evolution of low-salinity magmatic fluids at the porphyry to epithermal transition: a thermodynamic study. Mineral. Deposita 39, 864–889.
Herzig, P.M., Hannington, M.D., 1993. Gold mineralization in seafloor spreading centres of the Western Pacific. InterRidge News 2, 10–11.
Huston, D., Sie, S., Suter, G., Cooke, D., Both, R., 1995. Trace element in sulphide minerals from eastern Australian VHMS deposits: Part I. Proton microprobe analyses of pyrite, chalcopyrite, and sphalerite, and Part II. Selenium levels in pyrite: Comparison with the $\delta^{34}S$ values and implications for the source of sulphur in volcanogenic hydrothermal systems. Econ. Geol. 90, 1167–1196.
Jahn, B.M., Windley, B., Natal'in, B., Dobretsov, N., 2004. Phanerozoic continental growth in Central Asia. J. Asian Earth Sci. 23, 599–603.
Kesler, S.E., Chryssoulis, S.L., Simon, G., 2002. Gold in porphyry copper deposits: its abundance and fate. Ore Geol. Rev. 21, 103–124.
Kotlyar, I., Zhulanova, I., Rusakova, T., Gagieva, A., 2001. Isotopic Systems of the Magmatic and Metamorphic Complexes of Northeast Russia. North East Interdisciplinary Scientific Research Institute, Far East Branch, RAS, Magadan, pp. 319.
Kouzmanov, K., Bailly, L., Ramboz, C., Rouer, O., Beny, J.M., 2002. Morphology, origin and infrared microthermometry of fluid inclusions in pyrite from the Radka epithermal copper deposit, Srednogorie zone. Bulgaria. Mineral. Deposita 37, 599–613.
Kovalenker, V., Naumov, V., Prokof'ev, V.Y., Jelen, S., Gaber, M., 2006. Compositions of magmatic melts and evolution of mineral-forming fluids in the banska Stiavnica epithermal Au-Ag-Pb-Zn deposit, Slovakia: A study of inclusions in minerals. Geochem. Int. 44, 118–136.
Large, R.R., Danyushevsky, L., Hollit, C., Maslennikov, V., Meffre, S., Gilbert, S., Bull, S., Scott, R., Emsbo, P., Thomas, H., Singh, B., Foster, J., 2009. Gold and trace element zonation in pyrite using a laser imaging technique: implications for the timing of gold in orogenic and carlin-style sediment-hosted deposits. Econ. Geol. 104, 635–668.
Larocque, A.C., Hodgson, C., 1995. Effects of greenschist-facies metamorphism and related deformation on the Mobrun massive sulfide deposit, Quebec, Canada. Mineral. Deposita 30, 439–448.
Larocque, A.C., Hodgson, C.J., Cabri, L.J., Jackman, J.A., 1995. Ion-microprobe analysis of pyrite, chalcopyrite and pyrrhotite from the Mobrun VMS deposit in northwestern Quebec; evidence for metamorphic remobilization of gold. Can. Mineral. 33, 373–388.
Li, Z., Wang, X., Wang, H., Wu, G., 2008. Geology of the Sankuanggou gold–bearing iron–copper deposit in Nenjiang County, Heilongjiang Province. Geol. Resour. 3, 004.
Liu, J., Bai, X., Zhao, S., Tran, M., Zhang, Z., Zhao, Z., Zhao, H., Lu, J., 2011. Geology of the Sandaowanzi telluride gold deposit of the northern Great Xing'an Range, NE China: geochronology and tectonic controls. J. Asian Earth Sci. 41, 107–118.
Liu, W.Y., Cook, N.J., Ciobanu, C.L., Yu, L., Qiu, X.P., Chen, Y.C., 2016. Mineralogy of tin-sulfides in the Zijinshan porphyry-epithermal system, Fujian Province, China. Ore Geol. Rev. 72, 682–698.
Lobanov, K., Yakubchuk, A., Creaser, R.A., 2014. Besshi-Type VMS Deposits of the Rudny Altai (Central Asia). Econ. Geol. 109, 1403–1430.
Lockington, J.A., Cook, N.J., Ciobanu, C.L., 2014. Trace and minor elements in sphalerite from metamorphosed sulphide deposits. Mineral. Petrol. 108, 873–890.
Maddox, L., Bancroft, G.M., Scaini, M., Lorimer, J., 1998. Invisible gold: comparison of Au deposition on pyrite and arsenopyrite. Am. Mineral. 83, 1240–1245.
Mao, J.W., Pirajno, F., Lehmann, B., Luo, M.C., Berzina, A., 2014. Distribution of porphyry deposits in the Eurasian continent and their corresponding tectonic settings. J. Asian Earth Sci. 79, 576–584.
Mao, Y.J., Qin, K.Z., Li, C.S., Tang, D.M., 2015. A modified genetic model for the Huangshandong magmatic sulfide deposit in the Central Asian Orogenic Belt, Xinjiang, western China. Mineral. Deposita 50, 65–82.
Maydagán, L., Franchini, M., Lentz, D., Pons, J., McFarlane, C., 2013. Sulfide composition and isotopic signature of the Altar Cu-Au deposit, Argentina: constraints on the evolution of the porphyry-epithermal system. Can. Mineral. 51, 813–840.
Mills, S.E., Tomkins, A.G., Weinberg, R.F., Fan, H.R., 2015. Implications of pyrite geochemistry for gold mineralisation and remobilisation in the Jiaodong gold district, northeast China. Ore Geol. Rev. 71, 150–168.
Moggi-Cecchi, V., Cipriani, C., Rossi, P., Ceccato, D., Rudello, V., Somacal, H., 2002. Trace element contents and distribution maps of chalcopyrite: a micro-PIXE study. Per. Miner. 71, 101–109.
Müller, W., Shelley, M., Miller, P., Broude, S., 2009. Initial performance metrics of a new custom-designed ArF excimer LA-ICPMS system coupled to a two-volume laser-ablation cell. J. Anal. At. Spectrom. 24, 209–214.
Muntean, J.L., Cline, J.S., Simon, A.C., Longo, A.A., 2011. Magmatic-hydrothermal origin of Nevada/'s Carlin-type gold deposits. Nature Geosci. 4, 122–127.
Pacevski, A., Libowitzky, E., Zivkovic, P., Dimitrijevic, R., Cvetkovic, L., 2008. Copper-bearing pyrite from the Čoka Marin polymetallic deposit, Serbia: Mineral inclusions or true solid-solution? Can. Mineral. 46, 249–261.
Pang, X.Y., Qin, K.Z., Wang, L., Song, G.X., Li, G.M., Su, S.Q., Zhao, C., 2017. Deformation characteristics of the Tongshan fault within Tongshan porphyry copper deposit, Heilongjiang Province, and restoration of alteration zones and orebodies. Acta Petrol. Sinica 33 (2), 398–414.
Phillips, G., Powell, R., 2010. Formation of gold deposits: a metamorphic devolatilization model. J. Metamorph. Geol. 28, 689–718.
Pokrovski, G.S., Kara, S., Roux, J., 2002. Stability and solubility of arsenopyrite, FeAsS, in crustal fluids. Geochim. Cosmochim. Acta 66, 2361–2378.
Qin, K.Z., Sun, S., Li, J.L., Fang, T.G., Wang, S.L., Liu, W., 2002. Paleozoic epithermal Au and porphyry Cu deposits in North Xinjiang, China: epochs, features, tectonic linkage and exploration significance. Resour. Geol. 52, 291–300.
Qin, K.Z., Xiao, W.J., Zhang, L.C., Xu, X., Hao, J., Sun, S., Li, J., Tosdal, R.M., 2005. Eight stages of major ore deposits in northern Xinjiang, NW-China: clues and constraints on the tectonic evolution and continental growth of Central Asia. In: Mineral Deposit Research: Meeting the Global Challenge. Springer, pp. 1327–1330.
Radosavljevic, S.A., Stojanovic, J.N., Radosavljevic-Mihajlovic, A.S., Vukovic, N.S., 2016. (Pb-Sb)-bearing sphalerite from the Cumavici polymetallic ore deposit, Podrinje Metallogenic District, East Bosnia and Herzegovina. Ore Geol. Rev. 72, 253–268.
Ramsden, A., Kinealy, K., French, D., 1991. Gold grades and iron content of sphalerite-relationship of possible genetic significance from Hellyer volcanogenic massive-sulphide deposit of northwest Tasmania, Australia. Inst. Min. Metall. Trans. Section B. Appl. Earth Sci. 100.
Reich, M., Becker, U., 2006. First-principles calculations of the thermodynamic mixing properties of arsenic incorporation into pyrite and marcasite. Chem. Geol. 225, 278–290.
Reich, M., Kesler, S.E., Utsunomiya, S., Palenik, C.S., Chryssoulis, S.L., Ewing, R.C., 2005. Solubility of gold in arsenian pyrite. Geochim. Cosmochim. Acta 69, 2781–2796.
Reich, M., Deditius, A., Chryssoulis, S., Li, J.W., Ma, C.Q., Parada, M.A., Barra, F., Mittermayr, F., 2013a. Pyrite as a record of hydrothermal fluid evolution in a porphyry copper system: a SIMS/EMPA trace element study. Geochim. Cosmochim. Acta 104, 42–62.
Reich, M., Palacios, C., Barra, F., Chryssoulis, S., 2013b. "Invisible" silver in chalcopyrite and bornite from the Mantos Blancos Cu deposit, northern Chile. Eur. J. Mineral. 25, 453–460.
Seedorff, E., Dilles, J., Proffett, J., Einaudi, M., Zurcher, L., Stavast, W., Johnson, D., Barton, M., 2005. Porphyry deposits: characteristics and origin of hypogene features. Econ. Geol. 100th Anniversary 29, 251–298.
Sengör, A., Burtman, V., 1993. Evolution of the Altaid tectonic collage and Palaeozoic crustal growth in Eurasia. Nature 364, 299–307.
Shalaby, I.M., Stumpfl, E., Helmy, H.M., El Mahallawi, M.M., Kamel, O.A., 2004. Silver and silver-bearing minerals at the Um Samiuki volcanogenic massive sulphide deposit, Eastern Desert. Egypt. Miner. Deposita 39, 608–621.
Shen, P., Shen, Y.C., Liu, T.B., Zhu, H., Wang, L., Zeng, Q.D., Li, G.M., 2008. Prediction of hidden ore bodies using integrated geology, source of fluids and Stratagem EH4 geophysical survey in Kuoerzhenkuola gold deposit in Xinjiang. China. Resour. Geol. 58, 52–71.
Sillitoe, R.H., Hedenquist, J.W., 2003. Linkages Between Volcanotectonic Settings, Ore-fluid Compositions, and Epithermal Precious Metal Deposits. Society of Economic Geologists Special Publication 10, pp. 315–343.
Simon, G., Huang, H., Penner-Hahn, J.E., Kesler, S.E., Kao, L.-S., 1999. Oxidation state of gold and arsenic in gold-bearing arsenian pyrite. Am. Mineral. 84, 1071–1079.
Simon, G., Kesler, S.E., Essene, E.J., Chryssoulis, S.L., 2000. Gold in porphyry copper deposits: Experimental determination of the distribution of gold in the Cu-Fe-S system at 400 to 700 C. Econ. Geol. 95, 259–270.
Song, G.X., Qin, K.Z., Wang, L., Guo, J.H., Li, Z.Z., Tong, K.Y., Zou, X.Y., Li, G.M., 2015. Type, zircon U-Pb age and Paleo-volcano edifice of Zhengguang gold deposit in Duobaoshan orefield in Heilongjiang Province, NE-China. Acta Petrol. Sin. 31, 2402–2416 (in Chinese with English abstract).
Song, G.X., Qin, K.Z., Li, G.M., Wang, L., 2018. Basic characteristics and research progresses of intermediate sulfidation type epithermal gold polymetallic deposits, and prospects. Acta Petrol. Sin. 34 (3), 748–762 (in Chinese with English abstract).
Tan, C.Y., Wang, G.H., Li, Y.S., 2010. New progress and significance on the mineral exploration in Duobaoshan mineralization area, Heilongjiang, China. Geol. Bull. China 29 (2/3), 436–445 (in Chinese with English abstract).
Tauson, V., Kravtsova, R., Smagunov, N., Spiridonov, A., Grebenshchikova, V., Budyak, A., 2014. Structurally and superficially bound gold in pyrite from deposits of different genetic types. Russ. Geol. Geophys. 55, 273–289.
Tong, K.Y., Yang, Y.C., Song, G.X., Guo, J.H., Liang, H.J., Ma, L.F., 2015. Discussion on geological characteristics, ore genesis and prospecting of the Zhengguang Au-Zn deposit in Heilongjiang Province. Geol. Explor. 51, 507–518 (in Chinese with English abstract).
United States Geological Survey, 2014. Microanalytical Reference Materials and Accessories. United States Geological Survey. http://crustal.usgs.gov/ geochemical_reference_standards/microanalytical_RM.html (Viewed 6 October 2016).
Van Achterbergh, E., Ryan, C., Jackson, S., Griffin, W., 2001. Data reduction software for LA-ICP-MS. laser-ablation-ICPMS in the earth sciences—principles and applications. Miner. Assoc. Canada Short Course 29, 239–243.

Vaughan, J., Kyin, A., 2004. Refractory gold ores in Archaean greenstones, Western Australia: mineralogy, gold paragenesis, metallurgical characterization and classification. Mineral. Mag. 68, 255–277.
Vielreicher, N.M., Groves, D.I., McNaughton, N.J., 2016. The giant Kalgoorlie Gold Field revisited. Geosci. Front. 7, 359–374.
Vikentyev, I.V., 2006. Precious metal and telluride mineralogy of large volcanic-hosted massive sulfide deposits in the Urals. Mineral. Petrol. 87, 305–326.
Vikentyev, I.V., Yudovskaya, M.A., Mokhov, A.V., Kerzin, A.L., Tsepin, A.I., 2004. Gold and PGE in massive sulfide ore of the Uzelginsk deposit, southern Urals. Russia. Can. Mineral. 42, 651–665.
Voudouris, P.C., 2014. Hydrothermal corundum, topaz, diaspore and alunite supergroup minerals in the advanced argillic alteration lithocap of the Kassiteres-Sapes porphyry-epithermal system, western Thrace, Greece. Neues Jahrb. Mineral. Abh. 191, 117–136.
Wan, B., Zhang, L., Xiang, P., 2010. The ashele VMS type Cu-Zn deposit in Xinjiang, NW China formed in a rifted arc setting. Res. Geol. 60, 150–164.
Wang, L., Qin, K.Z., Song, G.X., Pang, X.Y., Li, Z.Z., Zhao, C., Jin, L.Y., Zou, X.Y., Li, G.M., 2018. Volcanic-subvolcanic rocks and tectonic setting of the Zhengguang intermediate sulfidation epithermal Au-Zn deposit, eastern Central Asian Orogenic Belt, NE China. J. Asian Earth Sci. 165, 328–351.
Wang, S.W., Zhou, H., 2009. Characteristics of primary ores in Zhengguang gold deposit. Helongjiang Land Res. 4, 68.
Wang, X.C., Wang, X.L., Wang, L., Liu, J.Y., Xia, B., Deng, J., Xu, X.M., 2007. Metallogeny and reformation of the Duobaoshan superlarge porphyry copper deposit in Heilongjiang. Chinese J. Geol. 42, 124–133 (in Chinese with English abstract).
Windley, B.F., Alexeiev, D., Xiao, W.J., Kroner, A., Badarch, G., 2007. Tectonic models for accretion of the Central Asian Orogenic Belt. J. Geol. Soc. 164, 31–47.
Wu, G., Chen, Y.C., Sun, F.Y., Liu, J., Wang, G.R., Xu, B., 2015. Geochronology, geochemistry, and Sr-Nd-Hf isotopes of the early Paleozoic igneous rocks in the Duobaoshan area, NE China, and their geological significance. J. Asian Earth Sci. 97, 229–250.
Wu, Z., Sun, Y., Wang, B., 2006. Geology and geochemistry of Zhengguang gold deposit, Heilongjiang province. Geol. Prospect. 42, 38–42 (in Chinese with English abstract).
Xiao, W.J., Kusky, T., 2009. Geodynamic processes and metallogenesis of the Central Asian and related orogenic belts: introduction. Gondwana Res. 16, 167–169.
Xiao, W., Santosh, M., 2014. The western Central Asian Orogenic Belt: a window to accretionary orogenesis and continental growth. Gondwana Res. 25, 1429–1444.
Xiao, W., Sun, M., Santosh, M., 2015. Continental reconstruction and metallogeny of the Circum-Junggar areas and termination of the southern Central Asian Orogenic Belt. Geosci. Front. 6, 137–140.
Xu, X.W., Cai, X.P., Qu, W.J., Song, B.C., Qin, K.Z., Zhang, B.L., 2006. Later Cretaceous granitic porphyritic Cu-Mo mineralization system in the Hongshan area, Northwestern Yunnan and its significances for tectonics. Acta Geol. Sin. 80, 1422–1433 (in Chinese with English abstract).
Yakubchuk, A., 2004. Architecture and mineral deposit settings of the Altaid orogenic collage: a revised model. J. Asian Earth Sci. 23, 761–779.
Zaw, K., Large, R.R., 1996. Petrology and geochemistry of sphalerite from the Cambrian VHMS deposits in the Rosebery-Hercules district, western Tasmania: Implications for gold mineralisation and Devonian metamorphic-metasomatic processes. Mineral. Petrol. 57, 97–118.
Zeng, Q.D., Liu, J.M., Chu, S.X., Wang, Y.B., Sun, Y., Duan, X.X., Zhou, L.L., Qu, W.J., 2014. Re-Os and U-Pb geochronology of the Duobaoshan porphyry Cu-Mo-(Au) deposit, northeast China, and its geological significance. J. Asian Earth Sci. 79, 895–909.
Zhang, J., Deng, J., Chen, H.Y., Yang, L.Q., Cooke, D., Danyushevsky, L., Gong, Q.J., 2014. LA-ICP-MS trace element analysis of pyrite from the Chang'an gold deposit, Sanjiang region, China: Implication for ore-forming process. Gondwana Res. 26, 557–575.
Zhao, C., Qin, K.Z., Song, G.X., Li, G.M., Li, Z.Z., Pang, X.Y., Wang, L., 2018. Petrogenesis and tectonic setting of ore-related porphyry in the Duobaoshan Cu deposit within the eastern Central Asian Orogenic Belt, Heilongjiang Province, NE China. J. Asian Earth Sci. 165, 352–370.
Zhao, Y., Huang, Y.H., Liang, K., Zhang, Q.N., 2016. Rare Earth Element and trace element features of auriferous pyrite in the Zhenyuan gold deposit, Sanjiang region, Yunnan Province. China. Acta Petrol. Sin. 31, 3297–3308 (in Chinese with English abstract).
Zhao, Y.Y., Wang, J.-P., Zhao, G.-J., Cui, Y.-B., 2011. Metallogenic regularity and prospecting direction of Duobaoshan ore field, Heilongjiang Province. China. J. Jilin Univ. (Earth Science Edition) 41, 1676–1688 (in Chinese with English abstract).
Zwahlen, C., Cioldi, S., Wagner, T., Rey, R., Heinrich, C., 2014. The porphyry Cu-(Mo-Au) deposit at Altar (Argentina): tracing gold distribution by vein mapping and LA-ICP-MS mineral analysis. Econ. Geol. 109, 1341–1358.